

World Journal of *Radiology*

World J Radiol 2022 September 28; 14(9): 319-351



ORIGINAL ARTICLE**Retrospective Study**

- 319 Reliability of ultrasound ovarian-adnexal reporting and data system amongst less experienced readers before and after training
Katlariwala P, Wilson MP, Pi Y, Chahal BS, Croutze R, Patel D, Patel V, Low G
- 329 Contrast-enhanced multidetector computed tomography features and histogram analysis can differentiate ameloblastomas from central giant cell granulomas
Ghosh A, Lakshmanan M, Manchanda S, Bhalla AS, Kumar P, Bhutia O, Mridha AR

LETTER TO THE EDITOR

- 342 Augmentation of literature review of COVID-19 radiology
Merchant SA, Nadkarni P, Shaikh MJS

ABOUT COVER

Peer Reviewer of *World Journal of Radiology*, Suleman A Merchant, MD, DMRD, MBBS, Professor, LTM General Hospital & Medical College, Sion, Mumbai 400022, India. suleman.a.merchant@gmail.com

AIMS AND SCOPE

The primary aim of *World Journal of Radiology* (*WJR*, *World J Radiol*) is to provide scholars and readers from various fields of radiology with a platform to publish high-quality basic and clinical research articles and communicate their research findings online.

WJR mainly publishes articles reporting research results and findings obtained in the field of radiology and covering a wide range of topics including state of the art information on cardiopulmonary imaging, gastrointestinal imaging, genitourinary imaging, musculoskeletal imaging, neuroradiology/head and neck imaging, nuclear medicine and molecular imaging, pediatric imaging, vascular and interventional radiology, and women's imaging.

INDEXING/ABSTRACTING

The *WJR* is now abstracted and indexed in PubMed, PubMed Central, Emerging Sources Citation Index (Web of Science), Reference Citation Analysis, China National Knowledge Infrastructure, China Science and Technology Journal Database, and Superstar Journals Database. The 2022 edition of Journal Citation Reports® cites the 2021 Journal Citation Indicator (JCI) for *WJR* as 0.48.

RESPONSIBLE EDITORS FOR THIS ISSUE

Production Editor: *Xiang-Di Zhang*; Production Department Director: *Xu Guo*; Editorial Office Director: *Jia-Ping Yan*.

NAME OF JOURNAL

World Journal of Radiology

ISSN

ISSN 1949-8470 (online)

LAUNCH DATE

January 31, 2009

FREQUENCY

Monthly

EDITORS-IN-CHIEF

Thomas J Vogl

EDITORIAL BOARD MEMBERS

<https://www.wjgnet.com/1949-8470/editorialboard.htm>

PUBLICATION DATE

September 28, 2022

COPYRIGHT

© 2022 Baishideng Publishing Group Inc

INSTRUCTIONS TO AUTHORS

<https://www.wjgnet.com/bpg/gerinfo/204>

GUIDELINES FOR ETHICS DOCUMENTS

<https://www.wjgnet.com/bpg/gerinfo/287>

GUIDELINES FOR NON-NATIVE SPEAKERS OF ENGLISH

<https://www.wjgnet.com/bpg/gerinfo/240>

PUBLICATION ETHICS

<https://www.wjgnet.com/bpg/gerinfo/288>

PUBLICATION MISCONDUCT

<https://www.wjgnet.com/bpg/gerinfo/208>

ARTICLE PROCESSING CHARGE

<https://www.wjgnet.com/bpg/gerinfo/242>

STEPS FOR SUBMITTING MANUSCRIPTS

<https://www.wjgnet.com/bpg/gerinfo/239>

ONLINE SUBMISSION

<https://www.f6publishing.com>

Retrospective Study

Reliability of ultrasound ovarian-adnexal reporting and data system amongst less experienced readers before and after training

Prayash Katlariwala, Mitchell P Wilson, Yeli Pi, Baljot S Chahal, Roger Croutze, Deelan Patel, Vimal Patel, Gavin Low

Specialty type: Radiology, nuclear medicine and medical imaging

Provenance and peer review:

Unsolicited article; Externally peer reviewed.

Peer-review model: Single blind

Peer-review report's scientific quality classification

Grade A (Excellent): 0
Grade B (Very good): B
Grade C (Good): C, C
Grade D (Fair): 0
Grade E (Poor): 0

P-Reviewer: Aydin S, Turkey;
Sahin H, Turkey

Received: March 12, 2022

Peer-review started: March 12, 2022

First decision: May 31, 2022

Revised: June 14, 2022

Accepted: September 13, 2022

Article in press: September 13, 2022

Published online: September 28, 2022



Prayash Katlariwala, Mitchell P Wilson, Yeli Pi, Baljot S Chahal, Roger Croutze, Deelan Patel, Vimal Patel, Gavin Low, Department of Radiology and Diagnostic Imaging, University of Alberta, Edmonton T6G 2B7, AB, Canada

Corresponding author: Prayash Katlariwala, BSc, Department of Radiology and Diagnostic Imaging, University of Alberta, 8440-112 Street NW, Edmonton T6G 2B7, AB, Canada. prayashvk@gmail.com

Abstract

BACKGROUND

The 2018 ovarian-adnexal reporting and data system (O-RADS) guidelines are aimed at providing a system for consistent reports and risk stratification for ovarian lesions found on ultrasound. It provides key characteristics and findings for lesions, a lexicon of descriptors to communicate findings, and risk characterization and associated follow-up recommendation guidelines. However, the O-RADS guidelines have not been validated in North American institutions or amongst less experienced readers.

AIM

To evaluate the diagnostic accuracy and inter-reader reliability of ultrasound O-RADS risk stratification amongst less experienced readers in a North American institution with and without pre-test training.

METHODS

A single-center retrospective study was performed using 100 ovarian/adnexal lesions of varying O-RADS scores. Of these cases, 50 were allotted to a training cohort and 50 to a testing cohort *via* a non-randomized group selection process in order to approximately equal distribution of O-RADS categories both within and between groups. Reference standard O-RADS scores were established through consensus of three fellowship-trained body imaging radiologists. Three PGY-4 residents were independently evaluated for diagnostic accuracy and inter-reader reliability with and without pre-test O-RADS training. Sensitivity, specificity, positive predictive value, negative predictive value (NPV), and area under the curve (AUC) were used to measure accuracy. Fleiss kappa and weighted quadratic (pairwise) kappa values were used to measure inter-reader reliability. Statistical significance was $P < 0.05$.

RESULTS

Mean patient age was 40 ± 16 years with lesions ranging from 1.2 to 22.5 cm. Readers demonstrated excellent specificities (85%-100% pre-training and 91%-100% post-training) and NPVs (89%-100% pre-training and 91%-100% post-training) across the O-RADS categories. Sensitivities were variable (55%-100% pre-training and 64%-100% post-training) with malignant O-RADS 4 and 5 Lesions pre-training and post-training AUC values of 0.87-0.95 and 0.94-0.98, respectively ($P < 0.001$). Nineteen of 22 (86%) misclassified cases in pre-training were related to mischaracterization of dermoid features or wall/septation morphology. Fifteen of 17 (88%) of post-training misclassified cases were related to one of these two errors. Fleiss kappa inter-reader reliability was 'good' and pairwise inter-reader reliability was 'very good' with pre-training and post-training assessment ($k = 0.76$ and 0.77 ; and $k = 0.77-0.87$ and $0.85-0.89$, respectively).

CONCLUSION

Less experienced readers in North America achieved excellent specificities and AUC values with very good pairwise inter-reader reliability. They may be subject to misclassification of potentially malignant lesions, and specific training around dermoid features and smooth *vs* irregular inner wall/septation morphology may improve sensitivity.

Key Words: Ovarian-adnexal reporting and data system; Ovary; Malignancy; Accuracy; Reliability; Ultrasound

©The Author(s) 2022. Published by Baishideng Publishing Group Inc. All rights reserved.

Core Tip: This study supports the applied utilization of the ovarian-adnexal reporting and data system (O-RADS) ultrasound risk stratification tool by less experienced readers in North America. **KEY RESULTS:** The O-RADS ultrasound risk stratification requires validation in less experienced North American readers; Excellent specificities (85%-100%), area under the curve values (0.87-0.98) and very good pairwise reliability can be achieved by trainees in North America regardless of formal pre-test training; Less experienced readers may be subject to down-grade misclassification of potentially malignant lesions and specific training about typical dermoid features and smooth *vs* irregular margins of ovarian lesions may help improve sensitivity.

Citation: Katlariwala P, Wilson MP, Pi Y, Chahal BS, Croutze R, Patel D, Patel V, Low G. Reliability of ultrasound ovarian-adnexal reporting and data system amongst less experienced readers before and after training. *World J Radiol* 2022; 14(9): 319-328

URL: <https://www.wjgnet.com/1949-8470/full/v14/i9/319.htm>

DOI: <https://dx.doi.org/10.4329/wjr.v14.i9.319>

INTRODUCTION

Building on the original ovarian-adnexal reporting and data system (O-RADS) publication in 2018, the American College of Radiology (ACR) O-RADS working group has recently introduced risk stratification and management recommendations to supplement the detailed reporting lexicon for this classification system[1,2]. These guidelines aim to provide consistent language, accurate characterization, and standardized recommendations for ovarian/adnexal lesions identified on ultrasound, ultimately improving the quality of communication between ultrasound examiners, referring clinicians and patients. A couple of recent papers have validated the use of the O-RADS system as an effective tool for the detection of ovarian malignancies, possessing high diagnostic accuracy and robust inter-reader reliability even without formalized training[3,4] For its future directions, the O-RADS working group specifically calls for additional studies validating this system in North American institutions and amongst less experienced readers[1]. Thus, the primary objective of the present study is to assess the inter-reader reliability of O-RADS classification amongst North American Radiology trainees using the O-RADS system, before and after training.

MATERIALS AND METHODS

This is a single center retrospective study performed at the University of Alberta Institutional Health

Research Ethics Board (HREB) approval was acquired prior to the study (Pro00097690). Patient consent for individual test cases was waived by the HREB as cases were retrospectively retrieved from the institutional Picture Archiving and Communication System (PACS) and de-identified prior to review by individual readers.

Patient selection

The University of Alberta institutional PACS was reviewed between May 2017 and July 2020 for all pelvic ultrasounds in adult female patients that demonstrated at least 1 ovarian/adnexal lesion with adequate diagnostic quality, including the presence of transvaginal 2D and Doppler sonographic image of the lesion(s) of interest. Studies were excluded if limited by technical factors such as bowel gas, large size of lesion, location of the adnexa, or inability to tolerate transvaginal ultrasound (O-RADS 0)[1].

A total of 100 diagnostic non-consecutive cases were selected by a Steering Committee of three authors including the senior author (Wilson MP, Patel V, Low G). In patients with more than one ovarian lesion, only different ipsilateral lesions were used with each individual lesion extracted as an independent blinded case when presented to study readers and the lesion of interest was designated with an arrow in each respective case. No concurrent contralateral lesions were used within the same patient. Cases were selected non-consecutively to acquire an approximately equal range of O-RADS 1 to O-RADS 5 Lesions. From these 100 cases, 50 cases were selected into separate 'Training' and 'Testing' groups. All cases were then de-identified leaving only the age, with 50 years of age used as a threshold for menopausal status. The cases were then listed as a teaching file in our institutional PACS (IMPAX 6 AGFA Healthcare) with a randomly assigned case number. All available static and cine imaging for the case were included in the teaching case file, with the additional inclusion of a 'key image' identifying the lesion intended for risk stratification with an arrow.

Training and testing

Three PGY-4 Diagnostic Radiology residents from a single institution volunteered as readers for the present study, henceforth referred to as R1, R2 and R3. The residents did not have prior formal experience with the O-RADS, SRU or IOTA systems for adnexal lesions, but have been exposed to ultrasonography in routine clinical practice totaling up to 12 wk. The residents were provided a copy of the O-RADS US Risk Stratification and Management System publication for independent review[1], and subsequently were asked to independently analyze all 50 'Testing' cases assigning the best O-RADS risk stratification score and lexicon descriptor. Answers were collected using an online Google Forms survey. Following completion of the testing file, an interval of six weeks was selected to prevent case recall. The senior author (Low G) then provided residents with a presentation reviewing the O-RADS system including lexicon descriptors, differentiating nuances for scoring, and separate examples of lesions in each O-RADS category (no overlap with cases used in the study design). The residents were then provided access to the 50 'Training' cases together with an answer key, for practice purposes and to establish familiarity with using the O-RADS system. Following the training session, and after the readers had reviewed the 'Training Cases,' the 50 "Testing" cases were then re-randomized, and independently scored again by all 3 readers in similar fashion to the pre-training format.

For both pre and post-training assessment, the reference gold standard was determined by independent consensus reading of three fellowship-trained body imaging radiologists with experience in gynaecologic ultrasound with 5, 13, and > 25 years of ultrasound experience (Wilson MP, Patel V, Low G).

Statistical analysis

The diagnostic accuracy of each individual reader and inter-observer variability between each reader both pre-training and post-training was evaluated. Continuous variables were expressed as the mean \pm standard deviation. Statistical tests included: Fleiss kappa (overall agreement) and weighted quadratic kappa (pairwise agreement) was used to calculate the inter-reader agreement. The kappa (κ) value interpretation as suggested by Cohen was used: $\kappa < 0.20$ (poor agreement), $\kappa = 0.21-0.40$ (fair agreement), $0.41-0.60$ (moderate agreement), $0.61-0.80$ (good agreement), and $0.81-1.00$ (very good agreement)[5]. Diagnostic accuracy measurements including sensitivity, specificity, positive predictive value (PPV) and negative predictive value (NPV) were calculated per O-RADS category for each individual reader. Receiver operating characteristic (ROC) analysis was used to evaluate the area under the receiver operating curve (AUC) for each reader. All statistical analyses were conducted using IBM SPSS (version 26) and MedCalc (version 19.6.1). A *P* value of < 0.05 was considered as statistically significant.

RESULTS

Cumulatively, the testing portion of the study was comprised of 50 cases. The average age of the patients in the test cohort was 40.1 ± 16.2 years and a range from 17 to 85 years. According to the reference standard, there were 10 cases (20%) of O-RADS 1, 10 cases (20%) of O-RADS 2, 7 cases (14%) of

Table 1 Sensitivity, specificity, positive predictive value and negative predictive value per ovarian-adnexal reporting and data system category for each reader on the pre-training assessment

Pre training	ORADS 1, %	ORADS 2, %	ORADS 3, %	ORADS 4, %	ORADS 5, %
Sensitivity					
R1	90 (55.5 to 99.8)	100 (69.5 to 100)	100 (59.0 to 100)	92 (61.5 to 99.8)	55 (23.4 to 83.3)
R2	90% (55.5 to 99.8)	100% (69.2 to 100)	71 (29.0 to 96.3)	92 (61.5 to 99.8)	82 (48.2 to 97.7)
R3	90 (55.5 to 99.8)	100 (69.2 to 100)	100 (59.0 to 100)	75 (42.8 to 94.5)	55 (23.4 to 83.3)
Specificity					
R1	100 (91.2 to 100)	85 (70.2 to 94.3)	98 (87.7 to 99.4)	100 (90.8 to 100)	100 (91.0 to 100)
R2	100 (91.2 to 100)	90 (76.3 to 97.2)	98 (87.7 to 99.4)	97 (86.2 to 99.9)	100 (91.0 to 100)
R3	98 (86.8 to 99.9)	90 (76.3 to 97.2)	95 (84.2 to 99.4)	95 (82.3 to 99.4)	100 (91.0 to 100)
PPV					
R1	100	63 (44.4 to 77.7)	88 (50.2 to 98.0)	100	100
R2	100	71 (49.7 to 86.4)	83 (40.5 to 97.4)	92 (61.2 to 98.7)	100
R3	90 (56.2 to 98.4)	71 (49.7 to 86.4)	78 (47.5 to 93.1)	82 (52.9 to 94.8)	100
NPV					
R1	98 (86.2 to 99.6)	100	100	97 (85.3 to 99.6)	89 (80.3 to 93.7)
R2	98 (86.2 to 99.6)	100	96 (86.7 to 98.6)	97 (85.0 to 99.6)	95 (84.8 to 98.6)
R3	98 (85.9 to 99.6)	100	100	93 (81.8 to 97.0)	89 (80.3 to 93.7)

O-RADS: Ovarian-Adnexal Reporting and Data System; PPV: Positive predictive value; NPV: Negative predictive value.

O-RADS 3, 12 cases (24%) of O-RADS 4 and 11 cases (22%) of O-RADS 5. Of the complete test cohort, 24 lesions (48%) were lateralized to the left and right with 2 lesions (4%) being located centrally in the pelvis and with an indeterminate origin site.

Overall, the lesion sizes ranged from 1.2 cm to 22.5 cm with an average size of 6.9 ± 4.7 . Mean lesion size by O-RADS category was: 2.1 ± 0.5 cm for O-RADS 1, 5.1 ± 1.4 cm for O-RADS 2, 10.6 ± 5.8 cm for O-RADS 3, 7.8 ± 4.6 cm for O-RADS 4 and 9.4 ± 4.4 cm for O-RADS 5 ($P < 0.001$).

Inter-reader reliability

The overall inter-reader agreement for the 3 readers as a group on the pre-training assessment was considered 'good' ($k = 0.76$ [0.68 to 0.84, 95% Confidence Interval {CI}], $p < 0.001$). Kappa values for agreement on individual O-RADS categories were 'good' or 'very good', as follows: O-RADS 1, $k = 0.82$ (0.66 to 0.98), $P < 0.001$; O-RADS 2, $k = 0.78$ (0.62 to 0.94), $P < 0.001$; O-RADS 3, $k = 0.74$ (0.58 to 0.90), $P < 0.001$; O-RADS 4, $k = 0.73$ (0.57 to 0.89), $P < 0.001$; O-RADS 5, $k = 0.72$ (0.56 to 0.88), $P < 0.001$.

The overall inter-reader agreement for the 3 readers as a group on the post-training assessment was considered 'good' ($k = 0.77$ [0.69 to 0.86, 95%CI], $P < 0.001$). Kappa values for agreement on individual O-RADS categories were 'good' or 'very good', as follows: O-RADS 1, $k = 0.96$ (0.80 to 1), $P < 0.001$; O-RADS 2, $k = 0.81$ (0.65 to 0.97), $P < 0.001$; O-RADS 3, $k = 0.65$ (0.49 to 0.81), $P < 0.001$; O-RADS 4, $k = 0.74$ (0.58 to 0.90), $P < 0.001$; O-RADS 5, $k = 0.70$ (0.54 to 0.86), $P < 0.001$.

Pairwise inter-reader agreement, as evaluated using weighted kappa, was 'very good', as follows: Pre-training: R1 and R2, $k = 0.79$ (0.62 to 0.96), $P < 0.001$; R1 and R3, $k = 0.77$ (0.59 to 0.95) $P < 0.001$; R2 and R3, $k = 0.87$ (0.73 to 1.00) $P < 0.001$. Post-training: R1 and R2, $k = 0.86$ (0.73 to 0.99), $P < 0.001$; R1 and R3, $k = 0.85$ (0.71 to 0.99) $P < 0.001$; R2 and R3, $k = 0.89$ (0.78 to 0.99) $P < 0.001$.

Diagnostic accuracy

The respective sensitivity, specificity, NPV, and PPV for each reader per O-RADS category are included in Table 1 for the pre-training assessment and Table 2 for the post-training assessment. All readers showed excellent specificities (85%-100% pre-training and 91%-100% post-training) and NPVs (89%-100% pre-training and 91%-100% post-training) across the O-RADS categories. Sensitivities range from 90%-100% in both pre-training and post-training for O-RADS 1 and O-RADS 2, 71%-100% pre-training and 86%-100% post-training for O-RADS 3, 75-92% in both pre-training and post-training for O-RADS 4, and 55%-82% pre-training and 64%-82% post-training for O-RADS 5. Readers misclassified 22 (14.7%) of 150 cases on pre-training assessment and 17 (11.3%) on post-training assessment. Misclassified cases and their respective lexicon descriptors are included in Table 3.

Table 2 The sensitivity, specificity, positive predictive value and negative predictive value per Ovarian-Adnexal Reporting and Data System category for each reader on the post-training assessment

Post training	ORADS 1, %	ORADS 2, %	ORADS 3, %	ORADS 4, %	ORADS 5, %
Sensitivity					
R1	100 (69.2 to 100)	100 (69.2 to 100)	100 (59 to 100)	92 (61.5 to 99.8)	73 (39 to 94)
R2	90 (55.5 to 99.8)	90 (55.5 to 99.8)	86 (42.1 to 99.6)	92 (61.5 to 99.8)	82 (48.2 to 97.7)
R3	100 (69.2 to 100)	100 (69.2 to 100)	100 (59 to 100)	75 (42.8 to 94.5)	64 (30.8 to 89.1)
Specificity					
R1	100 (91.2 to 100)	95 (83.1 to 99.4)	98 (87.7 to 99.9)	97 (86.2 to 99.9)	100 (91 to 100)
R2	100 (91.2 to 100)	98 (86.8 to 99.9)	93 (80.9 to 98.5)	95 (82.3 to 99.4)	100 (91 to 100)
R3	100 (91.2 to 100)	95 (83.1 to 99.4)	91 (77.9 to 97.4)	97 (86.2 to 99.9)	100 (91 to 100)
PPV					
R1	100	83 (56.4 to 95.1)	88 (50.2 to 98)	92 (61.2 to 98.7)	100
R2	100	90 (56.2 to 98.4)	67 (39.2 to 86.1)	85 (58.5 to 95.5)	100
R3	100	83 (56.4 to 95.1)	64 (40.8 to 81.7)	90 (55.9 to 98.5)	100
NPV					
R1	100	100	100	97 (85 to 99.6)	93 (83.2 to 97.2)
R2	98 (86.2 to 99.6)	98 (85.9 to 99.6)	98 (86.7 to 99.6)	97 (84.6 to 99.6)	95 (84.8 to 98.6)
R3	100	100	100	93 (82.2 to 97.1)	91 (81.7 to 95.5)

O-RADS: Ovarian-adnexal reporting and data system; PPV: Positive predictive value; NPV: Negative predictive value.

The ROC analysis evaluated diagnostic accuracy of the readers are included in [Figure 1A](#) for the pre-training assessment and [Figure 1B](#) for the post-training assessment. Given that higher O-RADS score (*i.e.* O-RADS 4 and O-RADS 5) are predictors of malignancy, reader AUC values are as follows: Pre-training: R1, AUC of 0.87 (0.75 to 0.95), $P < 0.001$; R2, AUC of 0.95 (0.84 to 0.99), $P < 0.001$; R3, AUC of 0.89 (0.77 to 0.96), $P < 0.001$. Post-training: R1, AUC of 0.96 (0.86 to 0.99), $P < 0.001$; R2, AUC of 0.98 (0.89 to 1.00), $P < 0.001$; R3, AUC of 0.94 (0.83 to 0.99), $P < 0.001$.

Pairwise comparison of the ROC curves showed a significant improvement post-training *vs* pre-training for R1 ($P = 0.04$) but not for R2 ($P = 0.29$) and R3 ($P = 0.21$).

DISCUSSION

This study demonstrates 'good' to 'very good' inter-reader agreement amongst less experienced readers in a North American institution, with pairwise and overall kappa values between spanning 0.76 and 0.89 ($P < 0.001$). The high degree of reliability is concordant with the findings of a prior study by Cao *et al*[4]. In their study performed at a tertiary care hospital and a cancer hospital in China, the pair-wise inter-reader agreement between a first-year radiology resident and a staff radiologist with 9 years experience in gynaecologic ultrasound was assessed. The authors found a kappa of 0.714 for the O-RADS system and a kappa of 0.77 for classifying lesion categories ($P < 0.001$).

Our study also highlights excellent diagnostic accuracies of resident readers when compared to a reference standard of three body-fellowship trained radiologists with experience in gynaecologic ultrasound. Solely with self-review of the O-RADS guidelines, the readers achieved high specificities greater than 0.85 and NPV greater than 0.89. These results persisted post-training, showing significant improvement in 1 resident ($P = 0.04$) and a trend towards improved accuracy amongst the other readers. The otherwise non-significant differences are due in part to excellent overall diagnostic accuracy without pre-test training as well as inadequate power to detect small differences. The study suggests that individual review of the O-RADS risk stratification is sufficient in less experienced readers with respect to specificity and AUC values. In this regard, this study validates the use of O-RADS risk classification amongst less experienced readers in a North American institution; a cohort specifically requiring validation by the ACR O-RADS committee[1].

An important risk amongst less experienced readers is the potential to misclassify potentially malignant lesions as benign. The sensitivity results in this study were variable in both pre-training and post-training assessment, particularly in higher O-RADS categories. In their respective pre-training and

Table 3 Misclassified ovarian-adnexal reporting and data system categories by readers in pre-training and post-training assessment

ORADS category	Reference standard lexicon descriptor	Misclassification category	Reader lexicon descriptor	Frequency of error in pre-training	Frequency of error in post-training
ORADS 1	Follicle defined as a simple cyst ≤ 3 cm	ORADS 2	Follicle defined as a simple cyst ≤ 3 cm	1	1
	Follicle defined as a simple cyst ≤ 3 cm	ORADS 2	Simple cyst > 5 cm but < 10 cm	1	0
	Follicle defined as a simple cyst ≤ 3 cm	ORADS 3	Multilocular cyst with smooth inner walls/septations < 10 cm, CS1-3	1	0
ORADS 2	simple cyst > 3 cm to 5 cm	ORADS 3	Unilocular cyst with irregular inner wall < 3mm height, any size	0	1
ORADS 3	Multilocular cyst with smooth inner walls/septations, < 10 cm, CS1-3	ORADS 2	Simple cyst > 5 cm but < 10 cm	1	0
	Multilocular cyst with smooth inner walls/septations, < 10 cm, CS1-3	ORADS 4	Multilocular cyst, irregular inner wall ± irregular septation	0	1
	Unilocular cyst (simple or non-simple) ≥ 10 cm	ORADS 4	Unilocular cyst with 1-3 papillary projections	1	0
ORADS 4	Multilocular cyst, irregular inner wall ± irregular septation	ORADS 1	Follicle defined as a simple cyst ≤ 3 cm	1	0
	Multilocular cyst, irregular inner wall ± irregular septation	ORADS 2	Classic benign lesion (hemorrhagic cyst < 10 cm)	1	0
	Multilocular cyst, irregular inner wall ± irregular septation	ORADS 3	Typical dermoid cyst, endometrioma, hemorrhagic cyst ≥ 10 cm	0	1
	Multilocular cyst, irregular inner wall ± irregular septation	ORADS 3	Multilocular cyst with smooth inner walls/septations < 10 cm, CS1-3	3	4
ORADS 5	Solid lesion with irregular outer contour	ORADS 2	Classic benign lesion (dermoid cyst < 10 cm)	10	4
	Solid lesion with irregular outer contour	ORADS 3	Solid lesion with smooth outer contour, any size, CS = 1	0	1
	Solid lesion with irregular outer contour	ORADS 3	Typical dermoid cyst, endometrioma, hemorrhagic cyst ≥ 10 cm	0	1
	Solid lesion with irregular outer contour	ORADS 4	Unilocular cyst with solid component	1	1
	Solid lesion with irregular outer contour	ORADS 4	Solid lesion with smooth outer contour, any size, CS = 2-3	0	2
	Multilocular cyst with solid component, CS3-4	ORADS 4	Multilocular cyst with solid component, CS1-2	1	0

O-RADS: Ovarian-adnexal reporting and data system; CS: Color scor.

post-training assessments, sensitivities were 64%-82% and 75%-92% for O-RADS 4 and 55%-82% and 64%-82% for O-RADS 5. The most frequent error on pre-training assessment was classifying a solid lesion as O-RADS 2 with a “typical dermoid cyst < 10 cm” lexicon descriptor. This error accounted for 45% (10/22) of misclassified cases in the pre-training assessment, with a reduction to 27% (4/17) of misclassified cases following training. This pitfall may be mitigated by comparing the hyperechoic component of a solid ovarian lesion to the surrounding pelvic and subcutaneous fat. The lesion should be classified as a dermoid only if it is isoechoic to the internal reference, and/or demonstrates one of three typical features including: (1) hyperechoic component with shadowing; (2) hyperechoic lines and dots; or (3) floating echogenic spherical structures[1,2]. In reviewing the test cases, all the solid lesions misclassified as dermoid had echogenicity lower than the intrapelvic fat. An example of this misclassification is shown in [Figure 2](#).

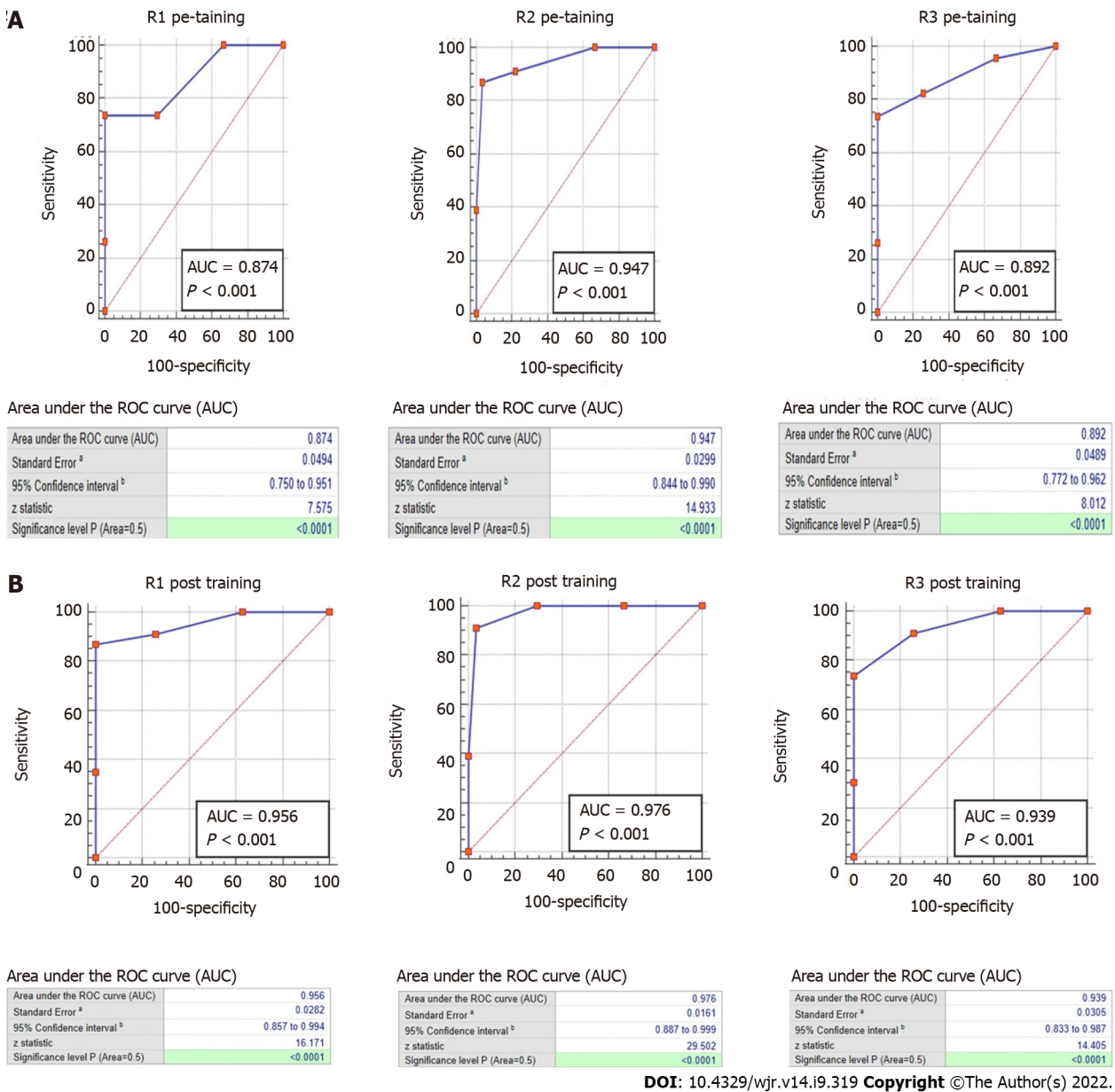
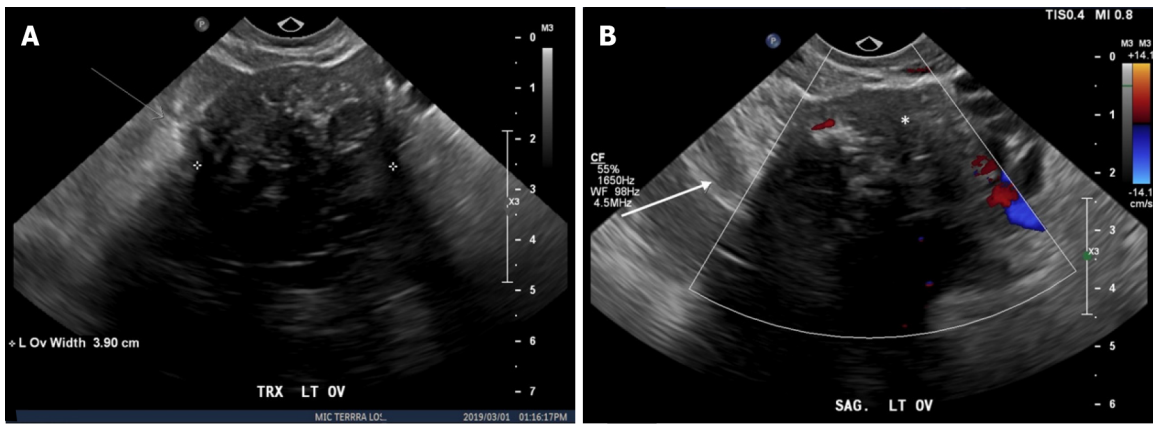


Figure 1 Receiver operating characteristic curve. A: Receiver operating characteristic (ROC) curve of each reader on the pre-training assessment; B: ROC curve of each reader on the post-training assessment. AUC: Area under the curve.

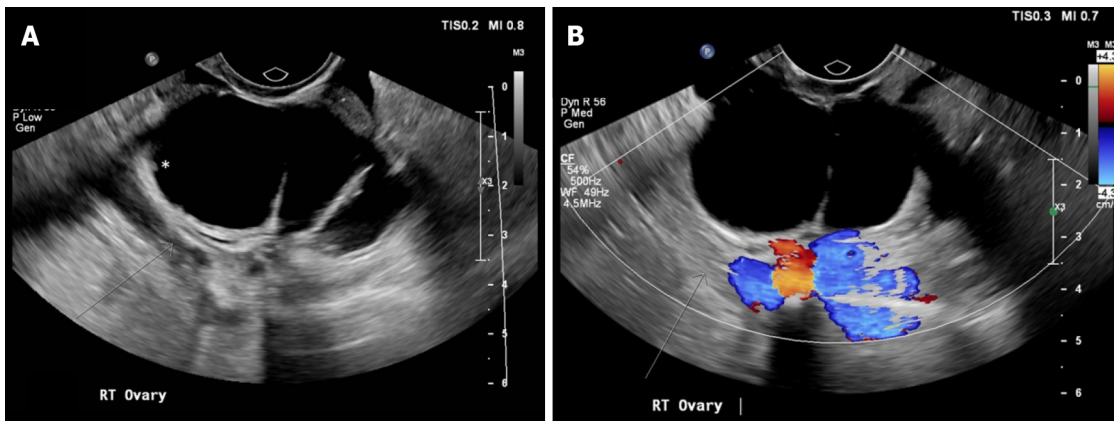
A second frequent error occurred in multilocular lesions with an irregular inner wall and/or irregular septation (O-RADS 4). These lesions were downgraded to O-RADS 1 through O-RADS 3 Lesions with variable lexicon descriptors used. Most commonly, these were characterized as a multilocular lesion with a smooth inner wall (O-RADS 3) in both pre-training and post-training assessment, suggesting that specific training on this finding was not sufficient in the current study. In this scenario, it is important that readers comprehensively evaluate the entire lesion on the cine clips, as irregularity in the inner wall/septation may be a subtle finding only seen in a small area within the lesion. An example of this misclassification is shown in [Figure 3](#). Unlike the dermoid misclassification, however, this downgrade still results in a recommendation for evaluation by an ultrasound specialist or MRI and gynecology referral, reducing the risk for adverse potential complication of this misclassification. Despite these misclassifications, the negative predictive value in O-RADS 4 and O-RADS 5 Lesions remains high in both pre-training and post-training assessment (89%-97% and 91%-97%).

This study is subject to several limitations Firstly, this was a retrospective non-consecutive review. As the menopausal status was often not provided in the clinical information, an arbitrary age cut-off of 50 years was used to differentiate pre-menopausal (< 50 years) vs post-menopausal patients (≥ 50 years), an approach has also been used in previous epidemiologic studies[6-8]. Secondly, we did not use a pathological reference standard. Our reference standard was an expert panel of 3 three fellowship-trained radiologists with experience in gynaecologic ultrasound. However, as O-RADS is a risk stratification system that is designed to be applied universally in the clinical setting and as our study is



DOI: 10.4329/wjr.v14.i9.319 Copyright ©The Author(s) 2022.

Figure 2 An example of a left ovarian solid lesion misclassified as a typical ovarian dermoid. A: Static gray-scale images; B: Static color Doppler ultrasound images. Static gray-scale and color Doppler ultrasound images shows a solid hypoechoic lesion with a non-uniform (irregular) margin demonstrated on the color Doppler image (Ovarian-Adnexal Reporting and Data System 5). The lesion demonstrates punctate echogenic areas (white asterisk) which are less echogenic than the surrounding pelvic fat (white arrow). Further, the echogenic areas do not fulfill one of the three descriptors required to characterize as a “typical dermoid cyst < 10 cm” according to ovarian-adnexal reporting and data system criteria (2). The hypoechoic lesion with posterior shadowing suggests a fibrous lesion.



DOI: 10.4329/wjr.v14.i9.319 Copyright ©The Author(s) 2022.

Figure 3 An example of a right ovarian cystic lesion misclassified as a “multilocular cyst < 10 cm, smooth inner wall, color score 1-3” (Ovarian-Adnexal Reporting and Data System 3). A: Static gray-scale images; B: Static color Doppler ultrasound images. Static gray-scale and color Doppler ultrasound images show a multilocular cyst with a subtle non-uniform (irregular) inner wall with solid components < 3 mm in height (white asterisk) (ovarian-adnexal reporting and data system 4) (2).

designed primarily to evaluate inter-reader agreement, an expert consensus panel is arguably a reasonable reference standard, and one that simulates ‘real world’ clinical practice. A similar approach has been taken in previous O-RADS accuracy studies[3,9]. Thirdly, our sample size of 50 training cases was fairly small. A large multi-center inter-observer variability study in North America would be useful to evaluate the generalizability of our findings. Despite these limitations, we believe that the rigorous study design and specific reader cohort provide valuable insight into a needed area of validation identified by the ACR O-RADS committee.

CONCLUSION

In summary, the study validated the use of the ACR-ORADS risk stratification system in less experienced readers, showing excellent specificities and AUC values when compared to a consensus reference standard and high pairwise inter-reader reliability. Less experienced readers may be at risk for misclassification of potentially malignant lesions, and specific training around common pitfalls may help improve sensitivity.

ARTICLE HIGHLIGHTS

Research background

The 2018 Ovarian-Adnexal Reporting and Data System (O-RADS) guidelines are aimed at providing a system for consistent reports and risk stratification for ovarian lesions found on ultrasound. It provides key characteristics and findings for lesions, a lexicon of descriptors to communicate findings, and risk characterization and associated follow-up recommendation guidelines. However, the O-RADS guidelines have not been validated in North American institutions.

Research motivation

The O-RADS ultrasound risk stratification requires validation in less experienced North American readers.

Research objectives

Evaluate the diagnostic accuracy and inter-reader reliability of ultrasound O-RADS risk stratification amongst less experienced readers in a North American institution without and with pre-test training.

Research methods

A single-center retrospective study was performed using 100 ovarian/adnexal lesions of varying O-RADS scores. Of these cases, 50 were allotted to a training cohort and 50 to a testing cohort *via* a non-randomized group selection process in order to approximately equal distribution of O-RADS categories both within and between groups. Reference standard O-RADS scores were established through consensus of three fellowship-trained body imaging radiologists. Three PGY-4 residents were independently evaluated for diagnostic accuracy and inter-reader reliability without and with pre-test O-RADS training. Sensitivity, specificity, positive predictive value, negative predictive value, and area under the curve (AUC) were used to measure accuracy. Fleiss kappa and weighted quadratic (pairwise) kappa values were used to measure inter-reader reliability.

Research results

Excellent specificities (85%-100%), AUC values (0.87-0.98) and very good pairwise reliability can be achieved by trainees in North America regardless of formal pre-test training. Less experienced readers may be subject to down-grade misclassification of potentially malignant lesions and specific training about typical dermoid features and smooth *vs* irregular margins of ovarian lesions may help improve sensitivity.

Research conclusions

Less experienced readers in North America achieved excellent specificities and AUC values with very good pairwise inter-reader reliability though they may be subject to misclassification of potentially malignant lesions. Training around dermoid features and smooth *vs* irregular inner wall/septation morphology may improve sensitivity.

Research perspectives

This study supports the applied utilization of the O-RADS ultrasound risk stratification tool by less experienced readers in North America.

FOOTNOTES

Author contributions: All authors contributed equally to the paper.

Supported by RSNA Research & Education Foundation Medical Student Grant #RMS2020.

Institutional review board statement: Institutional Health Research Ethics Board (HREB) approval was acquired from the University of Alberta prior to the study (Pro00097690).

Informed consent statement: Institutional ethics approval was obtained for this study which also waived the requirement for the informed consent. Please see institutional HREB approval document for details.

Conflict-of-interest statement: All authors have no conflicts of interest.

Data sharing statement: No additional data available.

Open-Access: This article is an open-access article that was selected by an in-house editor and fully peer-reviewed by external reviewers. It is distributed in accordance with the Creative Commons Attribution NonCommercial (CC BY-

NC 4.0) license, which permits others to distribute, remix, adapt, build upon this work non-commercially, and license their derivative works on different terms, provided the original work is properly cited and the use is non-commercial. See: <https://creativecommons.org/licenses/by-nc/4.0/>

Country/Territory of origin: Canada

ORCID number: Prayash Katlariwala [0000-0002-5822-1071](https://orcid.org/0000-0002-5822-1071); Mitchell P Wilson [0000-0002-1630-5138](https://orcid.org/0000-0002-1630-5138); Vimal Patel [0000-0003-2972-5980](https://orcid.org/0000-0003-2972-5980); Gavin Low [0000-0002-4959-8934](https://orcid.org/0000-0002-4959-8934).

S-Editor: Liu JH

L-Editor: A

P-Editor: Liu JH

REFERENCES

- 1 **Andreotti RF**, Timmerman D, Strachowski LM, Froyman W, Benacerraf BR, Bennett GL, Bourne T, Brown DL, Coleman BG, Frates MC, Goldstein SR, Hamper UM, Horrow MM, Hernanz-Schulman M, Reinhold C, Rose SL, Whitcomb BP, Wolfman WL, Glanc P. O-RADS US Risk Stratification and Management System: A Consensus Guideline from the ACR Ovarian-Adnexal Reporting and Data System Committee. *Radiology* 2020; **294**: 168-185 [PMID: [31687921](https://pubmed.ncbi.nlm.nih.gov/31687921/) DOI: [10.1148/radiol.2019191150](https://doi.org/10.1148/radiol.2019191150)]
- 2 **Andreotti RF**, Timmerman D, Benacerraf BR, Bennett GL, Bourne T, Brown DL, Coleman BG, Frates MC, Froyman W, Goldstein SR, Hamper UM, Horrow MM, Hernanz-Schulman M, Reinhold C, Strachowski LM, Glanc P. Ovarian-Adnexal Reporting Lexicon for Ultrasound: A White Paper of the ACR Ovarian-Adnexal Reporting and Data System Committee. *J Am Coll Radiol* 2018; **15**: 1415-1429 [PMID: [30149950](https://pubmed.ncbi.nlm.nih.gov/30149950/) DOI: [10.1016/j.jacr.2018.07.004](https://doi.org/10.1016/j.jacr.2018.07.004)]
- 3 **Pi Y**, Wilson MP, Katlariwala P, Sam M, Ackerman T, Paskar L, Patel V, Low G. Diagnostic accuracy and inter-observer reliability of the O-RADS scoring system among staff radiologists in a North American academic clinical setting. *Abdom Radiol (NY)* 2021; **46**: 4967-4973 [PMID: [34185128](https://pubmed.ncbi.nlm.nih.gov/34185128/) DOI: [10.1007/s00261-021-03193-7](https://doi.org/10.1007/s00261-021-03193-7)]
- 4 **Cao L**, Wei M, Liu Y, Fu J, Zhang H, Huang J, Pei X, Zhou J. Validation of American College of Radiology Ovarian-Adnexal Reporting and Data System Ultrasound (O-RADS US): Analysis on 1054 adnexal masses. *Gynecol Oncol* 2021; **162**: 107-112 [PMID: [33966893](https://pubmed.ncbi.nlm.nih.gov/33966893/) DOI: [10.1016/j.ygyno.2021.04.031](https://doi.org/10.1016/j.ygyno.2021.04.031)]
- 5 **Landis JR**, Koch GG. The measurement of observer agreement for categorical data. *Biometrics* 1977; **33**: 159-174 [PMID: [843571](https://pubmed.ncbi.nlm.nih.gov/843571/)]
- 6 **Phipps AI**, Ichikawa L, Bowles EJ, Carney PA, Kerlikowske K, Miglioretti DL, Buist DS. Defining menopausal status in epidemiologic studies: A comparison of multiple approaches and their effects on breast cancer rates. *Maturitas* 2010; **67**: 60-66 [PMID: [20494530](https://pubmed.ncbi.nlm.nih.gov/20494530/) DOI: [10.1016/j.maturitas.2010.04.015](https://doi.org/10.1016/j.maturitas.2010.04.015)]
- 7 **Hill K**. The demography of menopause. *Maturitas* 1996; **23**: 113-127 [PMID: [8735350](https://pubmed.ncbi.nlm.nih.gov/8735350/) DOI: [10.1016/0378-5122\(95\)00968-x](https://doi.org/10.1016/0378-5122(95)00968-x)]
- 8 **Im SS**, Gordon AN, Buttin BM, Leath CA 3rd, Gostout BS, Shah C, Hatch KD, Wang J, Berman ML. Validation of referral guidelines for women with pelvic masses. *Obstet Gynecol* 2005; **105**: 35-41 [PMID: [15625139](https://pubmed.ncbi.nlm.nih.gov/15625139/) DOI: [10.1097/01.AOG.0000149159.69560.ef](https://doi.org/10.1097/01.AOG.0000149159.69560.ef)]
- 9 **Basha MAA**, Metwally MI, Gamil SA, Khater HM, Aly SA, El Sammak AA, Zaitoun MMA, Khattab EM, Azmy TM, Alayouty NA, Mohey N, Almassry HN, Yousef HY, Ibrahim SA, Mohamed EA, Mohamed AEM, Afifi AHM, Harb OA, Algazzar HY. Comparison of O-RADS, GI-RADS, and IOTA simple rules regarding malignancy rate, validity, and reliability for diagnosis of adnexal masses. *Eur Radiol* 2021; **31**: 674-684 [PMID: [32809166](https://pubmed.ncbi.nlm.nih.gov/32809166/) DOI: [10.1007/s00330-020-07143-7](https://doi.org/10.1007/s00330-020-07143-7)]

Retrospective Study

Contrast-enhanced multidetector computed tomography features and histogram analysis can differentiate ameloblastomas from central giant cell granulomas

Adarsh Ghosh, Meyyappan Lakshmanan, Smita Manchanda, Ashu Seith Bhalla, Prem Kumar, Ongkila Bhutia, Asit Ranjan Mridha

Specialty type: Radiology, nuclear medicine and medical imaging

Provenance and peer review: Invited article; Externally peer reviewed.

Peer-review model: Single blind

Peer-review report's scientific quality classification

Grade A (Excellent): 0
Grade B (Very good): 0
Grade C (Good): C, C
Grade D (Fair): 0
Grade E (Poor): 0

P-Reviewer: Chen Q, China; Xie Q, China

Received: March 19, 2022

Peer-review started: March 19, 2022

First decision: June 16, 2022

Revised: July 5, 2022

Accepted: September 2, 2022

Article in press: September 2, 2022

Published online: September 28, 2022



Adarsh Ghosh, Department of Radiology, Children's Hospital of Philadelphia, Philadelphia, PA 19104, United States

Meyyappan Lakshmanan, Smita Manchanda, Department of Radiology, All India Institute of Medical Sciences, New Delhi 110029, India

Ashu Seith Bhalla, Department of Radiodiagnosis, All India Institute of Medical Sciences, New Delhi 110029, India

Prem Kumar, Ongkila Bhutia, Department of Oral & Maxillofacial Surgery, All India Institute of Medical Sciences, New Delhi 110029, India

Asit Ranjan Mridha, Department of Pathology, All India Institute of Medical Sciences, Ansari Nagar, New Delhi 110029, India

Corresponding author: Ashu Seith Bhalla, MD, Professor, Department of Radiodiagnosis, All India Institute of Medical Sciences, New Delhi 110029, India. ashubhalla1@yahoo.com

Abstract**BACKGROUND**

No qualitative or quantitative analysis of contrast-enhanced computed tomography (CT) images has been reported for the differentiation between ameloblastomas and central giant cell granulomas (CGCGs).

AIM

To describe differentiating multidetector CT (MDCT) features in CGCGs and ameloblastomas and to compare differences in enhancement of these lesions qualitatively and using histogram analysis.

METHODS

MDCT of CGCGs and ameloblastomas was retrospectively reviewed to evaluate qualitative imaging descriptors. Histogram analysis was used to compare the extent of enhancement of the soft tissue. Fisher's exact tests and Mann-Whitney *U* test were used for statistical analysis ($P < 0.05$).

RESULTS

Twelve CGCGs and 33 ameloblastomas were reviewed. Ameloblastomas had a predilection for the posterior mandible with none of the CGCGs involving the angle. CGCGs were multilocular (58.3%), with a mixed lytic sclerotic appearance (75%). Soft tissue component was present in 91% of CGCGs, which showed hyperenhancement (compared to surrounding muscles) in 50% of cases, while the remaining showed isoenhancement. Matrix mineralization was present in 83.3% of cases. Ameloblastomas presented as a unilocular (66.7%), lytic (60.6%) masses with solid components present in 81.8% of cases. However, the solid component showed isoenhancement in 63%. No matrix mineralization was present in 69.7% of cases. Quantitatively, the enhancement of soft tissue in CGCG was significantly higher than in ameloblastoma on histogram analysis ($P < 0.05$), with a minimum enhancement of > 49.05 HU in the tumour providing 100% sensitivity and 85% specificity in identifying a CGCG.

CONCLUSION

A multilocular, lytic sclerotic lesion with significant hyperenhancement in soft tissue, which spares the angle of the mandible and has matrix mineralization, should indicate prospective diagnosis of CGCG.

Key Words: Ameloblastoma; Granuloma; Giant cell; Multidetector CT

©The Author(s) 2022. Published by Baishideng Publishing Group Inc. All rights reserved.

Core Tip: Central giant cell granulomas (CGCGs) are rare tumours of the jaw. This study evaluated the findings of CGCGs on contrast-enhanced computed tomography in contrast with ameloblastomas, which are the most common tumours of the jaw in the developing world.

Citation: Ghosh A, Lakshmanan M, Manchanda S, Bhalla AS, Kumar P, Bhutia O, Mridha AR. Contrast-enhanced multidetector computed tomography features and histogram analysis can differentiate ameloblastomas from central giant cell granulomas. *World J Radiol* 2022; 14(9): 329-341

URL: <https://www.wjgnet.com/1949-8470/full/v14/i9/329.htm>

DOI: <https://dx.doi.org/10.4329/wjr.v14.i9.329>

INTRODUCTION

The most current World Health Organization classification of jaw tumours places giant cell granulomas under “giant cell lesions and simple bone cyst”. These include both central and peripheral giant cell granulomas[1]. Central giant cell granuloma (CGCG) usually appears as an expansile, multiloculated lesion with post-contrast enhancement and soft tissue extension[2-4]. Histologically it is characterized by focally distributed giant cells, spindle cells and possible areas of haemorrhage. A similar radiological and histopathological appearance may also be seen in brown tumours of hyperparathyroidism, and further clinical and laboratory correlation is required whenever aggressive, atypical or multiple CGCGs are seen[1,5]. CGCGs are slow-growing and insidious, although, increased rates of growth, presence of pain, tooth resorption or cortical erosions are considered signs of aggressive behaviour[2,3,6]. CGCGs are rare and tend to occur with a female preponderance in the second decade of life. Accelerated growth during pregnancy or following childbirth suggests hormone responsiveness of CGCGs. Although the exact pathophysiology of the tumour is yet to be elucidated: a reparative response to trauma, haemorrhagic products and inflammation is presumed to result in tumorigenesis. The classical lytic multilocular appearance of CGCGs on radiographs makes difficult their differentiation from ameloblastomas, odontogenic cyst, aneurysmal bone cysts, and odontogenic fibromas[3,7]. This differentiation is, however, vital because CGCGs are treated less aggressively (curettage, intralesional interferon, steroids or calcitonin injections[8]) as compared to other lesions with a similar radiological appearance. Ameloblastomas are by far is the most prevalent odontogenic tumour in the developing world[9], constituting about 14% of all jaw lesions[10]. Although benign, ameloblastomas exhibit an aggressive growth pattern, with up to 70% of cases[11] undergoing malignant transformation. It presents most frequently in males, in their third to fifth decades of life, as a slowly progressive swelling. The lesion favours the posterior mandible (63.15% of all cases as per one study[12]) and on imaging is a close differential of CGCGs with its unilocular or multilocular, lytic, expansive appearance[13]. Ameloblastomas are treated more radically and aggressively (with block resection, radiotherapy and vemurafenib[14]) vis-à-vis CGCGs making differentiation between the two crucial clinically.

Contrast-enhanced computed tomography (CT) can help characterise tumour biology better than noncontrast scans[15]. Although tumour location, appearance, contour and mass effect of the lesion on surrounding structures and teeth can be easily evaluated on noncontrast multidetector CT (MDCT)[4,7, 16,17] or on cone beam CT (CBCT), the presence of enhancing soft tissue and the extent of enhancement in the tumour can provide significant insight into tumour biology and can differentiate tumour types and pathological processes. For example, contrast-enhanced CT (CECT) helps differentiate purely cystic lesions of the jaw from cyst like lesions[18], a task relatively difficult on noncontrast MDCT or CBCT. Similarly, contrast-enhanced dynamic MDCT can help differentiate ameloblastomas[19] from other cystic jaw lesions, including keratocystic odontogenic tumours. Further quantification of the extent of tumour enhancement using histogram and texture analysis[20] can also characterise these tumours. However, to our knowledge, no qualitative or quantitative analysis of CECT images has been reported for the differentiation between ameloblastomas and CGCGs.

Given this background, we undertook this study to compare the MDCT features of CGCGs and ameloblastomas. More specifically we compared the utility of quantitative and qualitative evaluation of extent of tumour enhancement in differentiation of these two tumours.

MATERIALS AND METHODS

Subjects

The electronic records available from the Department of Pathology were searched to identify cases of CGCGs and ameloblastomas, between December 2016 and January 2019. All cases with MDCT images were included in the study, and six patients who did not have MDCT images were excluded. A total of 12 CGCGs and 33 ameloblastomas were identified and used in this study. The study was approved by the Institutional Ethics Committee (Ref No: IEC-622/03.07.2020, RP-31/2020).

Imaging technique

All MDCT acquisitions were performed either on a 64-MDCT scanner (Siemens SOMATOM Sensation, Erlangen, Germany) or 128-MDCT scanner (Siemens SOMATOM Definition Flash) available in our department. The images were acquired using 120 kV with automated tube current modulation, and a quality reference mAs of 80. A slice thickness of 0.6 mm was used. A 16-cm field of view, 512 × 512 matrix, was used to reconstruct data with routine 1mm sections being obtained using standard soft tissue and bone window kernels. CECT images were available for 38 of these 45 scans. Among these 38, venous phase images acquired at 60–70 s after intravenous injection were available in 35 patients (8 CGCGs and 27 ameloblastomas) [1–1.5 mL/kg of nonionic iodinated contrast (Iohexol 350 mg iodine/mL)]. Only arterial phase images were available as part of a head and neck angiography protocol in three patients. Noncontrast MDCT was available in seven patients.

Imaging interpretation

Two radiologists with 16 and 6 years' experience in head and neck imaging, blinded to clinical and pathological data reviewed all the MDCT scans in consensus. Nonconsensus was resolved by reviewing with a third radiologist. Zone-wise mapping of each lesion was done, as explained in Figure 1. Location of the lesion (mandible or maxilla); density (mixed, lytic or sclerotic as characterized on the bone window); multilocularity (unilocular with 1 or 2 thin septae; multilocular, honeycombing pattern); presence or absence of solid components; and erosion or thinning of the surrounding cortex were recorded. In mandibular lesions, the involvement of the angle (yes/no), and the status of the inferior alveolar canal was recorded (involvement/erosion) as well. The status of the overlying teeth (missing or root resorbed/present/adjoining roots displaced), and adjacent fat stranding and muscle thickening (present or absent) were noted. Venous phase images were evaluated ($n = 35$) to quantify the amount of soft tissue in each lesion (0–10%, 10%–25%, 25%–50%, 50%–75% and > 75%) and the type of enhancement of the solid component in the lesion were also characterised (purely cystic, hypoenhancing, isoenhancing, or hyperenhancing – the enhancement in these cases was compared to that of the surrounding muscles). Mineralisation of the tumour was recorded (absent, mineralised osteoid, thin bony septa, or thick septa with associated matrix). The three largest diameters of each lesion were recorded (along and perpendicular to the axis of mandible, and craniocaudal). These measurements were then used to derive the lesion's volume using the volume formula for an ellipsoid ($0.523 \times AP \times TR \times CC$).

Quantitative analysis of enhancement

The venous phase MDCT images were evaluated to compare the degree of enhancement between the tumours. Specifically, the contrast-enhanced MDCT images were opened on 3D Slicer 4.11.0 (<https://download.slicer.org/>). A freehand oval region of interest (ROI) measuring at least 1 cm in diameter was drawn on the largest bulk of the tumour, ensuring that the ROI was placed on soft tissue only, avoiding bony septa (Supplementary Figure 1). This was done by AG with 6 years' experience in

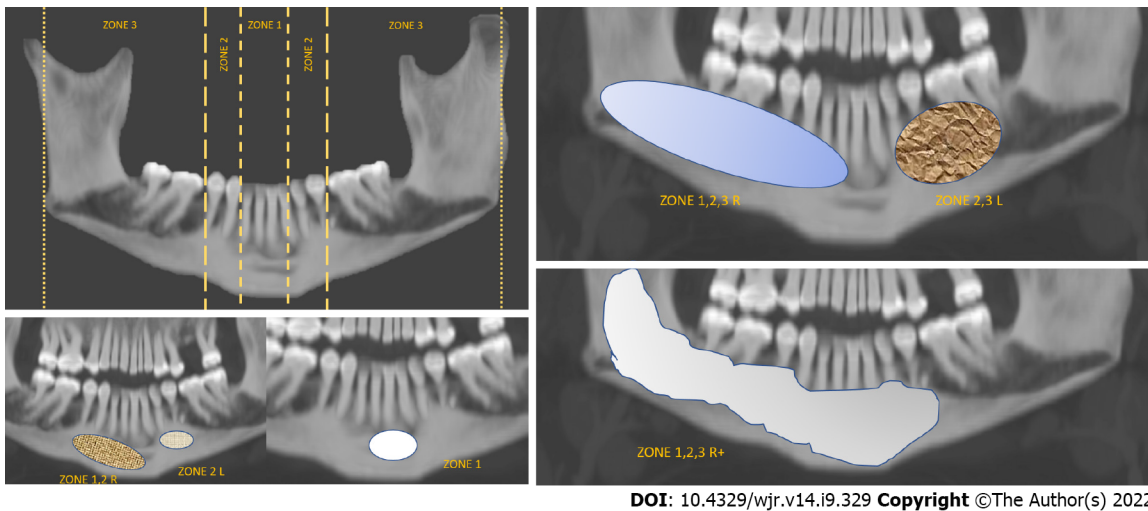


Figure 1 Location of every lesion was classified into the following zones: 1, limited to the incisors; 2, limited to the canine and premolars; and 3, limited to the molars and posterior mandible. A similar classification was applied to the maxilla. Lesions extending over multiple zones were classified as such, and a suffix of R or L was used to denote right or left-sided location. When the lesion crossed the midline across multiple zones, + was used to denote the same.

head and neck imaging and ROI placement was reviewed by SM. The pyRadiomics plugin (<https://pyradiomics.readthedocs.io/en/Latest/index.html>) was used to evaluate the histogram of the distribution of the HUs in the ROIs. Skewness, uniformity, entropy, kurtosis, and mean, median, maximum, minimum, 10th and 90th percentiles of the HU values in the histogram were evaluated. Purely cystic lesions ($n = 6$) were excluded from this analysis.

Statistical analysis

All data were tabulated and tested for normality when indicated. Continuous data were compared between the two data sets using the Mann–Whitney *U* test, while Fisher’s exact test was used to compare categorical data. $P < 0.05$ was considered statistically significant. Receiver operating characteristic (ROC) curve analysis was used to obtain the area under the curve (AUC) for texture parameters found to be significantly different between the two groups. Optimal cutoffs were obtained using bootstrapped Youden index. A leave-one-out cross-validation of the various enhancement parameters was done to evaluate generalisability.

RESULTS

A total of 12 CGCGs and 33 ameloblastomas were included in our study. The median age of patients with ameloblastoma was higher [35 years [95% confidence interval (CI) 28–48 years] as compared to patients with CGCG [29 years (95% CI 18–42 years)]; however, this was not significant ($P = 0.26$). Of the patients having ameloblastomas, 27.30% ($n = 9$) were female and 72.70% ($n = 24$) were male. The prevalence of CGCGs was nearly equal between the sexes: 41.70% ($n = 5$) in females *versus* 58.30% ($n = 7$) in males. This difference was again not significant.

Location

Both the pathologies favoured the mandible, with five ameloblastomas and four CGCGs appearing in the maxilla. CGCGs favoured a more central location with six lesions being located in zone 1 (50.00%), three in zone 2 (25.00%) and two in zone 3 (16.70%) (Table 1 and Figure 1). Only a single CGCG was large enough to involve zones 1, 2 and 3 simultaneously. This was significantly ($P < 0.0001$) different from ameloblastomas, which had a more varied distribution. Fourteen (42.40%) ameloblastomas were located exclusively in zone 3. Simultaneously, nine ameloblastomas were large enough to involve all three zones and two were large enough to cross the midline. Fifty per cent ($n = 14$ out of 28) of ameloblastomas had involvement of the angle of the mandible. In contrast, none of the CGCGs had this feature ($P = 0.013$).

Volume and size

Lesion volume was determined using the ellipsoid formula. CGCGs were significantly smaller in volume (median 10.31 cm³) as compared to ameloblastomas (median 35.9 cm³) ($P = 0.027$) (Table 2). ROC curve analysis and the associated cutoff are provided in Table 3. While there was considerable overlap

Table 1 Comparison of the various multidetector computed tomography imaging features between ameloblastoma and central giant cell granuloma

MDCT features		Pathology				Fisher's exact test (exact sig. two-sided)
		Ameloblastoma		CGCG		
		Count	% of all cases	Count	% of all cases	
Zone wise location (figure × for reference)	1, 2, 3	9	27.3 (14.4–43.9)	1	8.3 (0.9–32.8)	< 0.0001 ^a
	1	0	0.00%	6	50 (24.3–75.7)	
	1, 2	4	12.1 (4.2–26.3)	0	0.00%	
	2	0	0.00%	3	25 (7.6–52.9)	
	2,3	6	18.2 (8–33.7)	0	0.00%	
	3	14	42.4 (26.8–59.3)	2	16.7 (3.6–43.6)	
Density	Mixed	13	39.4 (24.2–56.4)	9	75 (47.1–92.4)	0.036 ^a
	Lytic	20	60.6 (43.6–75.8)	3	25 (7.6–52.9)	
Multilocularity; 1-Unilocular with 1 or 2 thin septae/2-Multilocular/3-Honeycombing	1	22	66.7 (49.7–80.8)	3	25 (7.6–52.9)	0.047 ^a
	2	8	24.2 (12.2–40.6)	7	58.3 (31.2–82)	
	3	3	9.1 (2.6–22.3)	2	16.7 (3.6–43.6)	
Bucco-lingual expansion	1	33	100.00%	12	100.00%	-
Solid component	Absent	6	18.2 (8–33.7)	1	8.3 (0.9–32.8)	0.309
	Present	27	81.8 (66.3–92)	11	91.7 (67.2–99.1)	
Cortical erosion	Thinning	1	3 (0.3–13.3)	1	8.3 (0.9–32.8)	1.000
	Erosion	32	97.86.7–99.7)	11	91.7 (67.2–99.1)	
Angle involved (of lesions in mandible)	No	14	50 (32.2–67.8)	8	100.00%	0.013 ^a
	Yes	14	50 (32.2–67.8)	0	0.00%	
Inferior alveolar canal displacement	No	3	14.3 (4.2–33.4)	2	25 (5.6–59.2)	0.597
	Yes	18	85.7 (66.6–95.8)	6	75 (40.8–94.4)	
Status of overlying teeth; Missing-0/Adjoining roots-1/Present-2	0	19	57.6 (40.7–73.2)	8	72.7 (43.5–91.7)	0.152
	1	12	36.4 21.6–53.4)	1	9.1 (1–35.3)	
	2	2	6.1 (1.3–18.1)	2	18.2 (4–46.7)	
Inferior alveolar canal erosion	No	2	9.5 (2–27.2)	3	37.5 (11.9–70.5)	0.112
	Yes	19	90.5 (72.8–98)	5	62.5 (29.5–88.1)	
Adjacent fat stranding	Absent	27	81.8 (66.3–92)	10	83.3 (56.4–96.4)	1.000
	Present	6	18.2 (8–33.7)	2	16.7 (3.6–43.6)	
Adjacent muscle thickening	Absent	26	78.8 (62.8–90)	11	91.7 (67.2–99.1)	0.419
	Present	7	21.2 (10–37.2)	1	8.3 (0.9–32.8)	
Extent of enhancement of soft tissue component in venous phase;	0	6	22.2 (9.8–40.2)	0	0.00%	

0-cystic/1- hypoenhancing/2- isoenhancing/3- hyperenhancing	2	17	63 (44.2–79.1)	4	50 (19.9–80.1)	0.013 ^a
	3	1	3.7 (0.4–16)	4	50 (19.9–80.1)	
	1	3	11.1 (3.2–26.8)	0	0.00%	
Amount of solid component	> 75%	9	33.3 (17.9–52.1)	6	75 (40.8–94.4)	0.061
	0- < 10%	8	29.6 (15.1–48.2)	0	0.00%	
	10%-25%	3	11.1 (3.2–26.8)	0	0.00%	
	25%-50%	5	18.5 (7.4–35.9)	0	0.00%	
	50%-75%	2	7.4 (1.6–21.7)	2	25 (5.6–59.2)	
Matrix mineralisation; Mineralised osteoid-1; Absent- 2; Thick septae with associated matrix-3; Thin bony septa- 4	1	1	3 (0.3–13.3)	3	25 (7.6–52.9)	0.004 ^a
	2	23	69.7 (52.9–83.2)	2	16.7 (3.6–43.6)	
	3	4	12.1 (4.2–26.3)	3	25 (7.6–52.9)	
	4	5	15.2 (6–30.1)	4	33.3 (12.5–61.2)	
Diameter		33	5.1(4.5–6)	12	3.7(2.1–4.8)	0.011 ^a
Volume		33	35.9 (23.05–47.59)	12	10.31 (3.67–59.37)	0.027 ^a

^aStatistically significant.

CGCG: Central giant cell granulomas; MDCT: Multidetector computed tomography.

Table 2 First-order histogram parameters comparing the extent of enhancement seen in the soft tissue component of ameloblastomas and central giant cell granulomas

		Ameloblastoma (n = 21); median (95%CI)	CGCG (n = 8); median(95%CI)	P value
Histogram parameter (n = 29)	Skewness	0.1 (-0.23–0.22)	0.07 (-0.51–0.47)	0.981
	Median (HU)	74.91 (56.97–93.24)	106.21 (95.1–134.52)	0.002
	Maximum (HU)	121.01 (100.11–150.05)	154.2 (133.42–183.09)	0.013
	90 percentile (HU)	95.32 (75.72–113.71)	137.43 (113.91–150.17)	0.001
	Entropy	1.62 (1.57–1.8)	1.5 (1.34–1.98)	0.487
	10 percentile (HU)	53.32 (34.2–71.13)	82.65 (74.86–116.64)	0.002
	Kurtosis	3.11 (2.71–3.54)	3.25 (2.69–4.08)	0.83
	Mean (HU)	74.06 (58.58–91.92)	106.95 (97.48–132.39)	0.002

CGCG: Central giant cell granulomas; CI: Confidence interval; MDCT: Multidetector computed tomography.

between the two volumes, a cutoff $\leq 13.04 \text{ cm}^3$ obtained 84.85% (68.1%–94.9%) specificity in identifying CGCG. Similarly, the diameter of ameloblastomas (measured along the long axis of the mandible) was higher than that of CGCGs with a cut off of $\leq 3.5 \text{ cm}$ (95%CI $\leq 2.1 \text{ cm}$ to $\leq 4.4 \text{ cm}$) providing 50% (95%CI 21.1%–78.9%) sensitivity and 90.91% (95%CI 75.7%–98.1%) specificity in identifying the latter.

Lesion appearance on bone window

60.6% of ameloblastomas were purely lytic (n = 20), as compared to only 25% of CGCGs (n = 3) (P = 0.047). A majority of all CGCGs (75%; n = 9) were predominantly mixed in appearance with both lytic and sclerotic components being present in the lesion. However, only 39.4% of ameloblastomas were mixed in appearance (n = 13). Neither of the tumours was purely sclerotic. Ameloblastomas (n = 22) were predominantly unilocular (66.7%) compared to 58.3% of CGCGs, which were multilocular. Matrix mineralisation in the form of osteoid, thin septa, or thick septa and associated dense matrix, was more common in CGCGs than ameloblastomas, where 70% showed no matrix mineralisation.

Table 3 Area under the curve of the various statistically significant histogram parameters of tumours in differentiating central giant cell granulomas from ameloblastomas

Variable	10 percentile	90 percentile	Mean	Median	Minimum
Area under the ROC curve (AUC)	0.863	0.875	0.863	0.869	0.887
5, 95%CI	0.685 to 0.962	0.699 to 0.968	0.685 to 0.962	0.692 to 0.965	0.714 to 0.974
Associated criterion (HU)	> 71.13	> 106.33	> 91.92	> 93.24	> 49.05
95%CI	> 66.43 to > 96.63	> 82.80 to > 113.71	> 88.68 to > 114.75	> 93.15 to > 110.22	> 48.51 to > 49.05
Sensitivity %	100 (63.1-100.0)	100 (63.1-100.0)	100 (63.1-100.0)	100 (63.1-100.0)	100 (63.1-100.0)
Specificity %	76.19 (52.8-91.8)	66.67 (43.0-85.4)	76.19 (52.8-91.8)	76.19 (52.8-91.8)	85.71 (63.7-97.0)
Leave-one out sensitivity %	100 (63.06-100)	100 (63.06-100)	100 (63.06-100)	100 (63.06-100)	100 (63.06-100)
Leave-one out specificity %	71.43 (47.82-88.72)	47.62 (25.71-70.22)	71.43 (47.82-88.72)	71.43 (47.82-88.72)	80.95 (58.09-94.55)

AUC: Area under the curve; CI: Confidence interval; ROC: Receiver operating characteristic.

Qualitative evaluation of contrast enhancement

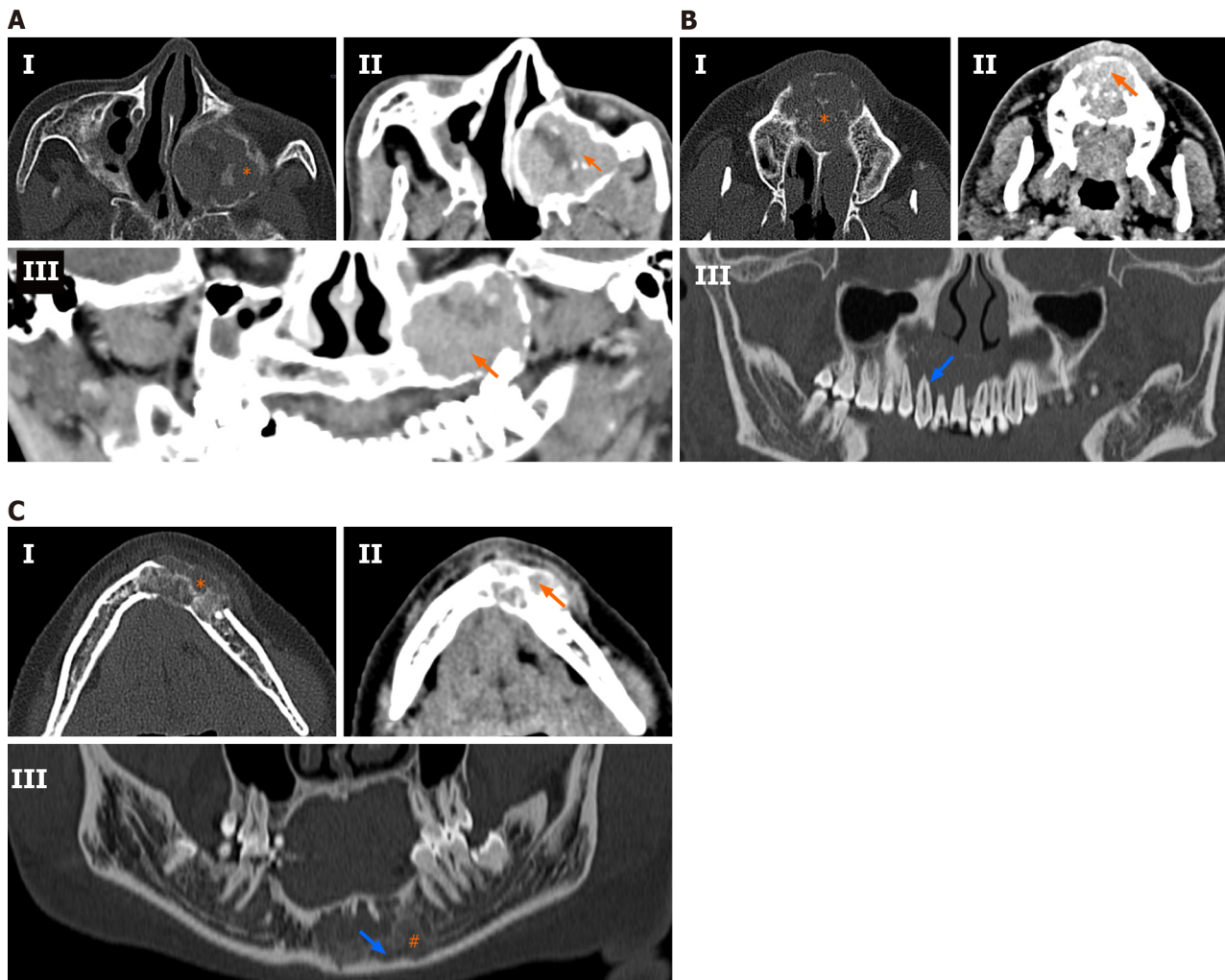
Evaluation of the degree of enhancement of solid component on venous phase images (8 CGCGs and 27 ameloblastomas) showed that six ameloblastomas were purely cystic with no solid component, and 17 (62.9%) ameloblastomas showed enhancement that was similar to the surrounding muscles. In comparison, four (50%) CGCGs showed enhancement higher than the surrounding muscles. This was significantly different ($P = 0.013$) from ameloblastomas, with only one ameloblastoma (3.7%) showing enhancement higher than muscles. These above findings are summarised in [Table 1](#) and [Figure 2](#).

Quantitative evaluation of enhancement

Histogram analysis (8 CGCGs and 21 ameloblastomas) of the enhancement of the solid component in the venous phase image was carried out after excluding the purely cystic lesions ($n = 6$). CGCGs had higher minimum, median, mean and maximum enhancement as compared to ameloblastomas ($P < 0.05$) on venous imaging ([Table 2](#)). A boot-strapped ROC curve analysis provided the AUC of the individual parameters as well as the optimum cutoffs. Minimum enhancement of > 49.0538 , had a sensitivity of 100% and a specificity of 85.71% in identifying a CGCC over ameloblastoma. The cutoffs, their associated sensitivity and specificity, and accuracy metrics of a leave-one-out cross-validation are provided in [Table 3](#).

DISCUSSION

We described the MDCT imaging features of CGCGs and contrasted them with ameloblastomas. Morphologically, both CGCGs and ameloblastomas had several overlapping features – making their differentiation difficult. Both ameloblastomas and CGCGs can be either unilocular or multilocular. Cortical expansion, cortical perforation, root displacement and root resorption are features suggestive of an aggressive variant of CGCG; however, these features are also present in ameloblastomas. MDCT or CBCT is preferred over radiography because it allows better evaluation of the bony anatomy, especially the integrity of the buccal and lingual cortex. MDCT with intravenous contrast allows better evaluation of the soft tissue component in these lesions. Location wise, we found that, although the CGCGs favoured the central jaw, up to 25% of the lesions were also found in the ramus[21,22]. Because of the small size of CGCGs, only one lesion was large enough to involve all the three zones. Ameloblastomas because of their larger sizes tended to involve more than one zone, with the most predominant preference for zone 3 (ramus of the mandible). This varied distribution is similar to that described in the literature[14,15]; involvement of the angle when present was highly specific for ameloblastoma. None of the CGCGs demonstrated the involvement of the angle. CGCGs were considerably smaller ($28.82 \pm 40.75 \text{ cm}^3$) in volume as compared to ameloblastomas ($66.18 \pm 84.33 \text{ cm}^3$) (Tables 2 and 3). Ameloblastomas are locally aggressive tumours, while CGCGs are slow-growing insidious masses that are sometimes known to regress spontaneously. Thus, the smaller volume of CGCG may be in keeping with the natural history of CGCGs ([Table 2](#)). Cortical expansion, cortical perforation, root displacement and root resorption as previously stated, can occur in both tumours[19,24-26]. Even in our series, there was no difference in the prevalence of root resorption, tooth displacement, cortical expansion or cortical perforation between the two entities ([Table 1](#)). CGCGs were predominantly multilocular (58.3%) with a unilocular appearance in only 25% of cases. In contrast, 67% of ameloblastomas were unilocular. Seventy-five percent of CGCGs



DOI: 10.4329/wjr.v14.i9.329 Copyright ©The Author(s) 2022.

Figure 2 Spectrum of multidetector computed tomography findings in central giant cell granulomas. A: 35-year-old woman presented with upper facial pain and nasal obstruction. Cone beam computed tomography (CBCT) shows a left-sided unilocular lytic lesion arising from the left maxilla (Panel I: Bone window) with compression of the maxillary sinus. Mineralised matrix was scattered in the substance of the tumour (asterisk). The lesion showed a significant soft tissue component, which enhanced to an extent greater than the surrounding muscles [arrow, Panel II and III: Axial and curved multiplanar reconstructed (MPR) coronal soft tissue images]. Hyperenhancement of the soft tissue tumour component was highly suggestive of a prospective central giant cell granuloma (CGCG) diagnosis; B: A 30-year-old man presented with pain and upper jaw swelling, contrast-enhanced computed tomography (CECT) showed a lytic sclerotic, multilocular mass arising from the maxilla with the presence of incomplete septae (asterisk) with mineralised matrix (Panel I: Axial bone window). Significant solid soft tissue component with enhancement greater (arrow) than the surrounding muscles was also noted (Panel II: Axial soft tissue window images). Curved MPR images (Panel III: Bone window) showed resorption of the roots (empty arrow) and floor of the nasal cavity; C: A 24-year-old woman presented with progressive jaw swelling over the last 6 mo, with intermittent pain. CECT showed a sclerotic lytic lesion with a honeycomb appearance (Panel I: Axial bone window) arising from the mandible. The lesion showed thick bony septae with mineralised matrix (asterisk). The associated soft tissue component showed enhancement similar to the surrounding muscles (orange arrow: Panel II: Axial soft tissue window). The tumour (blue arrow) can be seen encroaching onto the distal end (#) of the left inferior alveolar canal (Panel III: Curved MPR bone window).

showed both sclerotic and lytic components on the bone window, while 60% of ameloblastomas had a predominant lytic appearance (Figures 2 and 3). Additionally, the presence of osteoid either in the form of a mineralised matrix, thin bony septa or thick bony septa with dense mineralised matrix was a significant feature, and was present in 83% of CGCGs. In comparison, 70% of ameloblastomas had no mineralisation. Imaging features of ameloblastomas as contrasted with CGCGs are presented in Table 4 and Figures 2 and 3. Solid soft tissue was present in > 90% of all CGCGs, while 18% of ameloblastomas were purely lytic. The solid component of CGCGs showed avid enhancement in 50% of cases, while in the rest it showed enhancement similar to surrounding muscles, and only 4% of ameloblastomas showed hyperenhancement. On quantitative evaluation, we found that the solid components in CGCGs enhanced significantly greater than the solid tissue in ameloblastomas. Nackos *et al*[4] in their case series of seven CGCGs reported that the soft tissue in all the CGCGs showed avid contrast enhancement. Similarly, in our series, 50% of CGCGs showed enhancement greater than surrounding muscles, while the rest showed similar enhancement. While a mathematical discussion of each of the parameters used is beyond this paper's scope, briefly, entropy characterises the randomness of the distribution of the HU

Table 4 Summary of radiographic, multidetector computed tomography and magnetic resonance imaging findings in central giant cell granulomas and ameloblastomas

	Ameloblastoma	CGCG
Radiography	Posterior mandible; unilocular or multilocular; scalloped margins; root resorption, root displacement and bone expansion- may erode the cortex	Central mandible; multilocular sclerotic; root resorption, root displacement and bony expansion and cortical erosion
CBCT or MDCT	Mixed solid and cystic or purely cystic with thick enhancing rim or enhancing nodule (in unicystic variant)	Avid enhancement of soft tissue; mineralised matrix; better bony details
Our findings	Unilocular 66.7%; lytic 60.6%; solid component shows isoenhancement compared to surrounding muscles 63%; no matrix mineralisation in 69.7%	Multilocular 58.3%; mixed lytic sclerotic 75%; solid component shows hyperenhancement compared to surrounding muscles 50%; matrix mineralisation in 83.3%
MRI	T1 weighted - isointense; T2 weighted - hyperintense- cystic component; Heterogenous solid component	T1 weighted isointense; T2 weighted hyperintense to heterogeneous solid component

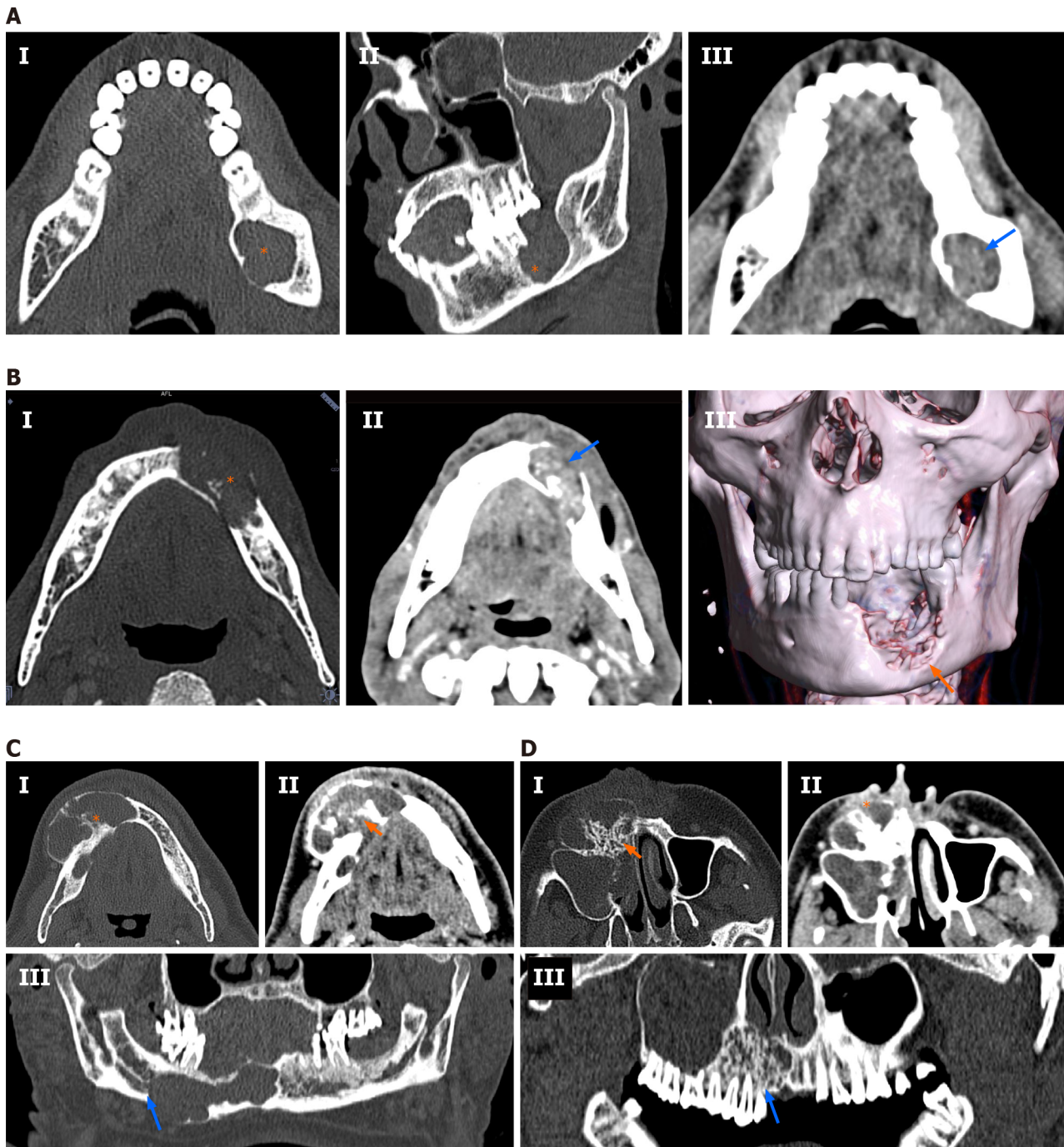
CBCT: Cone beam computed tomography; CGCG: Central giant cell granulomas; MDCT: Multidetector computed tomography; MRI: Magnetic resonance imaging.

values in the ROI. Skewness quantifies the asymmetry in the distribution of the HU values; meanwhile, kurtosis measures the histogram’s peak obtained from the HU values. A more detailed description can be read in the review by Lubner *et al*[23]. Histogram analysis showed that the mean, minimum and maximum enhancement of CGCGs was significantly higher than that of ameloblastomas (Tables 2 and 3). A cutoff > 49.05 HU for minimum enhancement in the tumour allowed 100% (63.1%-100.0%) sensitivity and 85.71% (63.7%-97.0%) specificity in differentiating CGCG from ameloblastoma.

The difference in enhancement patterns may be explained based on microvascular density (MVD) of these two tumours. While there are no studies directly comparing MVD of these two entities, separate studies have shown that ameloblastomas had an MVD of 14.9 ± 6 [27] compared to 24.5 ± 5.8 in CGCGs [28]. This difference, we hypothesise, would result in a faster and a more considerable peak enhancement in CGCGs than in ameloblastomas, which would then translate to differences in the maximum and minimum venous phase-contrast enhancement of CGCGs. Orthopantomography and CBCT only evaluate the morphology of tumours. Tumour vascularity, enhancement and MVD are important components of radiological tumour assessment and can be evaluated using contrast-enhanced MDCTs. Since in an index case, morphological imaging feature may overlap, the marked differences in enhancement may allow a confident prospective distinction between CGCGs and ameloblastomas.

CGCGs are rare tumours of the jaw making their prospective diagnosis difficult. The classical lytic multilocular appearance of CGCGs on radiographs makes their differentiation difficult from odontogenic cysts, aneurysmal bone cysts, odontogenic fibromas and ameloblastomas[3,7] (the most prevalent odontogenic tumours in the developing world[9]). However, this differentiation is vital because CGCGs are treated less aggressively (curettage, intralesional interferon, steroids or calcitonin injections[8]) compared to other lesions with a similar radiological appearance. We believe this is the unique value of our study, demonstrating the utility of CECT. We acknowledge that imaging alone cannot distinguish these lesions from their other mimics, including giant cell tumours and aneurysmal bone cysts. Moreover, because CGCGs are rare, prospective radiological diagnosis is often difficult and histopathological correlation is thus needed for definitive diagnosis. Sometimes, however, a pathological diagnosis may not be forthcoming[29], and in such cases, the radiological-pathological correlation becomes essential. We believe our findings would add value in such complex cases. Moreover, in patients due to multiple concurrent CGCGs[30] in patients with a mutation of the RAS/MAPK pathway[31], or underlying systemic illnesses, not all lesions undergo biopsy. In such patients, imaging would be valuable in follow-up and diagnosis. We believe contrast-enhanced MDCT would be invaluable in work-up and management of such cases.

This study had several limitations. Of a broad potential range of lytic lesions of the jaw, we compared only ameloblastomas and CGCGs. In our routine practice, we have seen that ameloblastomas have several overlapping imaging features with CGCGs. This, compounded with the rarity of CGCGs, makes their prospective identification difficult. Given the rarity of CGCGs, we decided to contrast the imaging and enhancement characteristics of CGCGs with its most common mimic in the jaw. The retrospective design of the study, with an asymmetric dataset, might have prevented the demonstration of more variations in the imaging features of CGCGs. Because of these limitations, further prospective studies are required to investigate the imaging characteristics and enhancement features of CGCGs, ameloblastomas and their various mimics.



DOI: 10.4329/wjr.v14.i9.329 Copyright ©The Author(s) 2022.

Figure 3 Spectrum of multidetector computed tomography findings in ameloblastoma. A: A 30-year-old man presented with progressive left lower jaw swelling. Cone beam computed tomography (CBCT) showed a unilocular, lytic lesion (asterisk) with no septae involving the left angle of the mandible (Panel I and II: Axial and coronal bone window). The soft tissue component showed enhancement similar (blue arrow) to the surrounding muscles (Panel III: Axial soft tissue window); B: A 52-year-old man with lower mid jaw pain and swelling; contrast-enhanced computed tomography (CECT) showed a sclerotic, lytic multilocular lesion with thin incomplete septae (asterisk) and associated mineralised matrix (Panel I: Axial bone window). There was a significant soft tissue component showing enhancement (blue arrow) similar to the surrounding muscles (Panel II: Axial soft tissue window). Erosion of the buccal cortex was seen in three-dimensional volume-rendered images (Panel III); C: A 53-year-old man with painful progressive lower jaw swelling of 7 mo duration. CECT showed a lytic sclerotic multilocular mandibular mass with multiple thick septae (asterisk), cortical expansion and breach (Panel I: Axial bone window). The solid component present in the tumour showed hypoenhancement (arrow) compared to the surrounding muscles (Panel II: Axial soft tissue window). Hypoenhancing soft tissue was characteristically not seen in central giant cell granulomas, allowing a prospective diagnosis of ameloblastoma. Erosion of the right canal of the inferior alveolar nerve (blue arrow) was clearly seen [Panel III: Curved multiplanar coronal reconstruction (MPR), bone window]; D: A 42-year-old man with upper maxillary swelling and significant malar pain. CECT showed a lytic sclerotic mass with honeycombing (orange arrow) and thick bony septae (Panel I: Axial bone window). There was significant cortical expansion with extension into the right maxillary sinus. The mass was predominantly lytic with minimal solid component (asterisk) seen in the mass, hypoenhancing compared to the surrounding muscles (Panel II: Axial soft tissue window). Erosion of the roots (blue arrow) with honeycomb appearance was visible (Panel III: Curved MPR coronal bone window).

CONCLUSION

Significant hyperenhancement of the soft tissue component on CECT in a jaw tumour may allow a prospective diagnosis of CGCG, especially in a multilocular lytic sclerotic centrally located jaw tumour with matrix mineralisation.

ARTICLE HIGHLIGHTS

Research background

Contrast-enhanced multidetector computed tomography (MDCT) can provide unique information about ameloblastomas and central giant cell granulomas (CGCGs).

Research motivation

To evaluate contrast-enhanced multidetector computed tomography (MDCT) features of ameloblastomas and CGCGs.

Research objectives

To describe differentiating MDCT features in CGCGs and ameloblastomas and to compare the differences in the enhancement of these two lesions qualitatively and using histogram analysis.

Research methods

MDCTs of CGCGs and ameloblastomas were retrospectively reviewed to evaluate qualitative imaging descriptors. Histogram analysis was used to compare the extent of enhancement of the soft tissue. Fisher's exact test and Mann-Whitney *U* test were used for statistical analysis ($P < 0.05$).

Research results

Twelve CGCGs and 33 ameloblastomas were reviewed. Ameloblastomas had a predilection for the posterior mandible with none of the CGCGs involving the angle. CGCGs were multilocular (58.3%), with a mixed lytic sclerotic appearance (75%). Soft tissue component was present in 91% of CGCGs, which showed hyperenhancement (compared to surrounding muscles) in 50% of cases, while the remaining showed isoenhancement. Matrix mineralisation was present in 83.3% of cases. Ameloblastomas presented as a unilocular (66.7%), lytic (60.6%) masses with solid components present in 81.8% of cases. However, the solid component showed isoenhancement in 63%. No matrix mineralisation was present in 69.7% of cases. Quantitatively, the enhancement of soft tissue in CGCGs was significantly higher than in ameloblastomas on histogram analysis ($P < 0.05$), with a minimum enhancement of > 49.05 HU in the tumour, providing 100% sensitivity and 85% specificity in identifying CGCG.

Research conclusions

A multilocular, lytic sclerotic lesion with significant hyperenhancing soft tissue component, which spares the angle of the mandible and has matrix mineralisation, should indicate a prospective diagnosis of CGCG.

Research perspectives

Future studies can evaluate the role of perfusion imaging for differentiating these two tumour types.

FOOTNOTES

Author contributions: Ghosh A contributed to methodology, software; Ghosh A and Lakshmanan M contributed to writing - original draft; Lakshmanan M contributed to investigation; Bhalla AS and Manchanda S contributed to conceptualization; Bhalla AS, Manchanda S, Kumar P, Bhutia O, and Mridha AR contributed to writing - review & editing, supervision; Kumar P, Bhutia O, and Mridha AR contributed to resources.

Institutional review board statement: The study was reviewed and approved by the All India Institute of Medical Science, New Delhi Institutional Review Board [(Approval No.IEC-622/03.07.2020, RP-31/2020)].

Informed consent statement: The requirement of signed consent forms was waived by the Institutional Ethics Board.

Conflict-of-interest statement: All the authors declare that they have no conflict of interest.

Data sharing statement: No additional data are available.

Open-Access: This article is an open-access article that was selected by an in-house editor and fully peer-reviewed by external reviewers. It is distributed in accordance with the Creative Commons Attribution NonCommercial (CC BY-NC 4.0) license, which permits others to distribute, remix, adapt, build upon this work non-commercially, and license their derivative works on different terms, provided the original work is properly cited and the use is non-commercial. See: <https://creativecommons.org/licenses/by-nc/4.0/>

Country/Territory of origin: India

ORCID number: Ashu Seith Bhalla [0000-0003-2200-2544](https://orcid.org/0000-0003-2200-2544).

S-Editor: Liu JH

L-Editor: Kerr C

P-Editor: Liu JH

REFERENCES

- 1 WHO histological classification of tumours of the oral cavity and oropharynx [DOI: [10.1007/978-2-287-92246-6_11](https://doi.org/10.1007/978-2-287-92246-6_11)]
- 2 **Flanagan AM**, Speight PM. Giant cell lesions of the craniofacial bones. *Head Neck Pathol* 2014; **8**: 445-453 [PMID: [25409853](https://pubmed.ncbi.nlm.nih.gov/25409853/) DOI: [10.1007/s12105-014-0589-6](https://doi.org/10.1007/s12105-014-0589-6)]
- 3 **Etöz M**, Asantogrol F, Akyol R. Central giant cell granulomas of the jaws: retrospective radiographic analysis of 13 patients. *Oral Radiol* 2020; **36**: 60-68 [PMID: [30825099](https://pubmed.ncbi.nlm.nih.gov/30825099/) DOI: [10.1007/s11282-019-00380-7](https://doi.org/10.1007/s11282-019-00380-7)]
- 4 **Nackos JS**, Wiggins RH 3rd, Harnsberger HR. CT and MR imaging of giant cell granuloma of the craniofacial bones. *AJNR Am J Neuroradiol* 2006; **27**: 1651-1653 [PMID: [16971606](https://pubmed.ncbi.nlm.nih.gov/16971606/)]
- 5 **Abdel Razek AA**. Computed tomography and magnetic resonance imaging of maxillofacial lesions in renal osteodystrophy. *J Craniofac Surg* 2014; **25**: 1354-1357 [PMID: [24902107](https://pubmed.ncbi.nlm.nih.gov/24902107/) DOI: [10.1097/SCS.0000000000000819](https://doi.org/10.1097/SCS.0000000000000819)]
- 6 **Triantafyllidou K**, Venetis G, Karakinaris G, Iordanidis F. Central giant cell granuloma of the jaws: a clinical study of 17 cases and a review of the literature. *Ann Otol Rhinol Laryngol* 2011; **120**: 167-174 [PMID: [21510142](https://pubmed.ncbi.nlm.nih.gov/21510142/) DOI: [10.1177/000348941112000305](https://doi.org/10.1177/000348941112000305)]
- 7 **Dunfee BL**, Sakai O, Pistey R, Gohel A. Radiologic and pathologic characteristics of benign and malignant lesions of the mandible. *Radiographics* 2006; **26**: 1751-1768 [PMID: [17102048](https://pubmed.ncbi.nlm.nih.gov/17102048/) DOI: [10.1148/rg.266055189](https://doi.org/10.1148/rg.266055189)]
- 8 **Pogrel AM**. The diagnosis and management of giant cell lesions of the jaws. *Ann Maxillofac Surg* 2012; **2**: 102-106 [PMID: [23482697](https://pubmed.ncbi.nlm.nih.gov/23482697/) DOI: [10.4103/2231-0746.101325](https://doi.org/10.4103/2231-0746.101325)]
- 9 **Lasisi TJ**, Adisa AO, Olusanya AA. Appraisal of jaw swellings in a Nigerian tertiary healthcare facility. *J Clin Exp Dent* 2013; **5**: e42-e47 [PMID: [24455050](https://pubmed.ncbi.nlm.nih.gov/24455050/) DOI: [10.4317/jced.51011](https://doi.org/10.4317/jced.51011)]
- 10 **Brown NA**, Betz BL. Ameloblastoma: A Review of Recent Molecular Pathogenetic Discoveries. *Biomark Cancer* 2015; **7**: 19-24 [PMID: [26483612](https://pubmed.ncbi.nlm.nih.gov/26483612/) DOI: [10.4137/BIC.S29329](https://doi.org/10.4137/BIC.S29329)]
- 11 **Odukoya O**, Effiom OA. Clinicopathological study of 100 Nigerian cases of ameloblastoma. *Niger Postgrad Med J* 2008; **15**: 1-5 [PMID: [18408774](https://pubmed.ncbi.nlm.nih.gov/18408774/)]
- 12 **Agbaje JO**, Olumuyiwa Adisa A, Ivanova Petrova M, Adenike Olusanya A, Osayomi T, Ajibola Effiom O, Oladele Soyele O, Gbenga Omitola O, Babajide Olawuyi A, Obos Okiti R, Eziafa Saiki T, Fomete B, Aremu Ibikunle A, Okwuosa C, Abimbola Olajide M, Mofoluwake Ladeji A, Emmanuel Adebisi K, Mobola Emmanuel M, Sikiru Lawal H, Uwadia E, Oludare Fakuade B, Mohammed Abdullahi Y, Politis C. Biological profile of ameloblastoma and its location in the jaw in 1246 Nigerians. *Oral Surg Oral Med Oral Pathol Oral Radiol* 2018; **126**: 424-431 [PMID: [30126803](https://pubmed.ncbi.nlm.nih.gov/30126803/) DOI: [10.1016/j.oooo.2018.06.014](https://doi.org/10.1016/j.oooo.2018.06.014)]
- 13 **Cadavid AMH**, Araujo JP, Coutinho-Camillo CM, Bologna S, Junior CAL, Lourenço SV. Ameloblastomas: current aspects of the new WHO classification in an analysis of 136 cases. *Surg Exp Pathol* 2019 [DOI: [10.1186/s42047-019-0041-z](https://doi.org/10.1186/s42047-019-0041-z)]
- 14 **Effiom OA**, Ogundana OM, Akinshipo AO, Akintoye SO. Ameloblastoma: current etiopathological concepts and management. *Oral Dis* 2018; **24**: 307-316 [PMID: [28142213](https://pubmed.ncbi.nlm.nih.gov/28142213/) DOI: [10.1111/odi.12646](https://doi.org/10.1111/odi.12646)]
- 15 **Malignant Tumours Involving the Jaws**. In: Atlas of Oral and Maxillofacial Radiology [Internet]. Chichester, UK: John Wiley & Sons, Ltd; 2017 [DOI: [10.1002/9781118939604.ch11](https://doi.org/10.1002/9781118939604.ch11)]
- 16 **Meyer KA**, Bancroft LW, Dietrich TJ, Kransdorf MJ, Peterson JJ. Imaging characteristics of benign, malignant, and infectious jaw lesions: a pictorial review. *AJR Am J Roentgenol* 2011; **197**: W412-W421 [PMID: [21862767](https://pubmed.ncbi.nlm.nih.gov/21862767/) DOI: [10.2214/AJR.10.7225](https://doi.org/10.2214/AJR.10.7225)]
- 17 **Özgür A**, Kara E, Arpacı R, Arpacı T, Esen K, Kara T, Duce MN, Apaydın FD. Nonodontogenic mandibular lesions: differentiation based on CT attenuation. *Diagn Interv Radiol* 2014; **20**: 475-480 [PMID: [25297390](https://pubmed.ncbi.nlm.nih.gov/25297390/) DOI: [10.5152/dir.2014.14143](https://doi.org/10.5152/dir.2014.14143)]
- 18 **Hayashi K**, Tozaki M, Sugisaki M, Yoshida N, Fukuda K, Tanabe H. Dynamic multislice helical CT of ameloblastoma and odontogenic keratocyst: correlation between contrast enhancement and angiogenesis. *J Comput Assist Tomogr* 2002; **26**: 922-926 [PMID: [12488736](https://pubmed.ncbi.nlm.nih.gov/12488736/) DOI: [10.1097/00004728-200211000-00011](https://doi.org/10.1097/00004728-200211000-00011)]
- 19 **Apajalahti S**, Kelppe J, Kontio R, Hagström J. Imaging characteristics of ameloblastomas and diagnostic value of computed tomography and magnetic resonance imaging in a series of 26 patients. *Oral Surg Oral Med Oral Pathol Oral Radiol* 2015; **120**: e118-e130 [PMID: [26166034](https://pubmed.ncbi.nlm.nih.gov/26166034/) DOI: [10.1016/j.oooo.2015.05.002](https://doi.org/10.1016/j.oooo.2015.05.002)]
- 20 **Oda M**, Staziaki PV, Qureshi MM, Andreu-Arasa VC, Li B, Takumi K, Chapman MN, Wang A, Salama AR, Sakai O. Using CT texture analysis to differentiate cystic and cystic-appearing odontogenic lesions. *Eur J Radiol* 2019; **120**: 108654

- [PMID: 31539792 DOI: 10.1016/j.ejrad.2019.108654]
- 21 **Jadu FM**, Pharoah MJ, Lee L, Baker GI, Allidina A. Central giant cell granuloma of the mandibular condyle: a case report and review of the literature. *Dentomaxillofac Radiol* 2011; **40**: 60-64 [PMID: 21159917 DOI: 10.1259/dmfr/85668294]
 - 22 **Hosur MB**, Puranik RS, Vanaki SS, Puranik SR, Ingaleshwar PS. Clinicopathological profile of central giant cell granulomas: An institutional experience and study of immunohistochemistry expression of p63 in central giant cell granuloma. *J Oral Maxillofac Pathol* 2018; **22**: 173-179 [PMID: 30158768 DOI: 10.4103/jomfp.JOMFP_260_17]
 - 23 **Lubner MG**, Smith AD, Sandrasegaran K, Sahani DV, Pickhardt PJ. CT Texture Analysis: Definitions, Applications, Biologic Correlates, and Challenges. *Radiographics* 2017; **37**: 1483-1503 [PMID: 28898189 DOI: 10.1148/rg.2017170056]
 - 24 **Meng Y**, Zhao YN, Zhang YQ, Liu DG, Gao Y. Three-dimensional radiographic features of ameloblastoma and cystic lesions in the maxilla. *Dentomaxillofac Radiol* 2019; **48**: 20190066 [PMID: 31124699 DOI: 10.1259/dmfr.20190066]
 - 25 **Ariji Y**, Morita M, Katsumata A, Sugita Y, Naitoh M, Goto M, Izumi M, Kise Y, Shimozato K, Kurita K, Maeda H, Ariji E. Imaging features contributing to the diagnosis of ameloblastomas and keratocystic odontogenic tumours: logistic regression analysis. *Dentomaxillofac Radiol* 2011; **40**: 133-140 [PMID: 21346078 DOI: 10.1259/dmfr/24726112]
 - 26 **Stavropoulos F**, Katz J. Central giant cell granulomas: a systematic review of the radiographic characteristics with the addition of 20 new cases. *Dentomaxillofac Radiol* 2002; **31**: 213-217 [PMID: 12087437 DOI: 10.1038/sj.dmfr.4600700]
 - 27 **ArabSheibani M**, Seifi S, Salehinejad J, Bijani A. Expression of CD34, VEGFR3 and eosinophil density in selected odontogenic tumors- a pilot study. *J Oral Biol Craniofac Res* 2020; **10**: 367-371 [PMID: 31687323 DOI: 10.1016/j.jobcr.2019.09.003]
 - 28 **Sadri D**, Shahsavari F, Hezarkhani M, Shafizadeh M. Expression of CD34 and CD31 in Central and Peripheral Giant Cell Granulomas. *J Dent (Shiraz)* 2019; **20**: 10-15 [PMID: 30937331 DOI: 10.30476/DENTJODS.2019.44557]
 - 29 **Upadhyaya JD**, Cohen DM, Islam MN, Bhattacharyya I. Hybrid Central Odontogenic Fibroma with Giant Cell Granuloma like Lesion: A Report of Three Additional Cases and Review of the Literature. *Head Neck Pathol* 2018; **12**: 166-174 [PMID: 28785965 DOI: 10.1007/s12105-017-0845-7]
 - 30 **Edwards PC**, Fox J, Fantasia JE, Goldberg J, Kelsch RD. Bilateral central giant cell granulomas of the mandible in an 8-year-old girl with Noonan syndrome (Noonan-like/multiple giant cell lesion syndrome). *Oral Surg Oral Med Oral Pathol Oral Radiol Endod* 2005; **99**: 334-340 [PMID: 15716842 DOI: 10.1016/j.tripleo.2004.08.021]
 - 31 **van den Berg H**, Schreuder WH, de Lange J. Multiple central giant cell tumour lesions are exclusively linked to syndromes related to RAS/MAPK pathway anomalies. *Int J Oral Maxillofac Surg* 2017; **46**: 1354-1355 [PMID: 28499505 DOI: 10.1016/j.ijom.2017.04.013]

Augmentation of literature review of COVID-19 radiology

Suleman Adam Merchant, Prakash Nadkarni, Mohd Javed Saifullah Shaikh

Specialty type: Radiology, nuclear medicine and medical imaging

Provenance and peer review:

Unsolicited article; Externally peer reviewed.

Peer-review model: Single blind

Peer-review report's scientific quality classification

Grade A (Excellent): 0

Grade B (Very good): B, B

Grade C (Good): C, C, C

Grade D (Fair): 0

Grade E (Poor): 0

P-Reviewer: Konovalov AB, Russia; Schoenhagen P, United States; Taydas O, Turkey; Zhu JB, China

Received: December 14, 2021

Peer-review started: December 14, 2021

First decision: March 7, 2022

Revised: March 26, 2022

Accepted: August 21, 2022

Article in press: August 21, 2022

Published online: September 28, 2022



Suleman Adam Merchant, LTM Medical College & LTM General Hospital, Mumbai 400022, Maharashtra, India

Prakash Nadkarni, College of Nursing, University of Iowa, Iowa City, IA 52242, United States

Mohd Javed Saifullah Shaikh, Department of Radiology, North Bengal Neuro Centre - Jupiter MRI & Diagnostic Centre, Siliguri 734003, West Bengal, India

Corresponding author: Suleman Adam Merchant, MBBS, MD, Chairman, LTM Medical College & LTM General Hospital, Sion Hospital, Mumbai 400022, Maharashtra, India.
suleman.a.merchant@gmail.com

Abstract

We suggest an augmentation of the excellent comprehensive review article titled "Comprehensive literature review on the radiographic findings, imaging modalities, and the role of radiology in the coronavirus disease 2019 (COVID-19) pandemic" under the following categories: (1) "Inclusion of additional radiological features, related to pulmonary infarcts and to COVID-19 pneumonia"; (2) "Amplified discussion of cardiovascular COVID-19 manifestations and the role of cardiac magnetic resonance imaging in monitoring and prognosis"; (3) "Imaging findings related to fluorodeoxyglucose positron emission tomography, optical, thermal and other imaging modalities/devices, including 'intelligent edge' and other remote monitoring devices"; (4) "Artificial intelligence in COVID-19 imaging"; (5) "Additional annotations to the radiological images in the manuscript to illustrate the additional signs discussed"; and (6) "A minor correction to a passage on pulmonary destruction".

Key Words: COVID-19 radiological findings; Chest radiographs; Hamptons hump; Westermark sign; Computed tomography; Cardiac magnetic resonance imaging; COVID-19-associated coagulopathy; COVID-19 imaging; Artificial intelligence in COVID-19

©The Author(s) 2022. Published by Baishideng Publishing Group Inc. All rights reserved.

Core Tip: Utility of classical radiographic findings suggestive of coronavirus disease 2019 (COVID-19) mediated pulmonary infarction (Hampton’s hump, Westermark sign, subpleural sparing and reversed halo sign) should improve the diagnostic accuracy of identification of COVID-19 pulmonary complications. This gain in accuracy would apply whether these findings are seen on plain chest X-ray or computed tomography. The former is important in financially constrained locales with limited medical technology infrastructure. Distinctive COVID-19-associated coagulopathy is more frequent with worsening disease severity in COVID-19. Cardiac magnetic resonance imaging can play an important role in monitoring and prognosis. “Artificial intelligence in COVID-19” and “‘Intelligent edge’ and other remote monitoring devices” are also discussed.

Citation: Merchant SA, Nadkarni P, Shaikh MJS. Augmentation of literature review of COVID-19 radiology. *World J Radiol* 2022; 14(9): 342-351

URL: <https://www.wjgnet.com/1949-8470/full/v14/i9/342.htm>

DOI: <https://dx.doi.org/10.4329/wjr.v14.i9.342>

TO THE EDITOR

We compliment Pal *et al*[1] for their excellent review. It is a comprehensive review indeed. An excellent effort with great details, including in depth pathophysiology, detailed illustrations, *etc.* Their coverage of imaging modalities is quite extensive too and includes a detailed look into the role of ultrasound in coronavirus disease 2019 (COVID-19), including point-of-care ultrasound, an invaluable addition. For the benefit of your readers, we wish to augment their excellent work and submit the following suggestions for the benefit of your readers.

INCLUSION OF ADDITIONAL RADIOLOGIC FEATURES

We are involved in an ongoing multicentric international study on COVID-19 chest imaging and developing artificial intelligence (AI) algorithms for diagnosis, risk stratification, monitoring, prognostication, *etc.* Our 2020 publication has described additional important and distinctive COVID-19 chest-imaging features[2]. These include the following, seen on both plain chest radiographs and computed tomography (CT).

Classic signs of pulmonary infarcts

Hampton’s hump: Triangular/wedge shaped opacities with their bases towards the periphery of the lung/lobe/lobule. This sign has sensitivity and specificity of 22% and 82%, respectively[3,4].

Westermark sign: Oligemia, a rarefied area due to blood vessel collapse, distal to the site of occlusion by a pulmonary embolus. This sign has sensitivity and specificity of 14% and 92%, respectively[3,5].

Palla’s sign: An enlarged right pulmonary artery, suggesting embolism of segmental/subsegmental pulmonary arteries when seen together with Westermark sign. Sensitivity is reported to be “low” and specificity unknown. These findings are likely due to the microvascular thrombosis propensity in COVID-19[6-8], as discussed below, leading to a relatively increased incidence of pulmonary thromboembolism in COVID-19 pneumonia patients[9].

It is time to revisit these time-tested radiological signs for pulmonary infarcts[2]. Utilizing classic signs of infarcts and pneumonia will increase diagnostic accuracy and help raise awareness about the utility of chest radiographs, even in the current era; especially in cost-constrained locales lacking sophisticated infrastructure. It will also help develop more accurate AI algorithms for diagnosis/prognosis of COVID-19. Co-occurrences of these signs are uncommon across COVID-19 patients: When seen in tandem, however, they may constitute a highly specific diagnostic signature. This speculation, of course, needs validation by larger studies.

SIGNS ASSOCIATED WITH COVID-19 PNEUMONIA

Subpleural sparing

Reported in 23% of COVID-19 cases in an Iranian study[10], subpleural sparing is commonly associated with nonspecific interstitial pneumonia and is described with lung contusions, pulmonary alveolar proteinosis, severe acute respiratory syndrome (SARS) and *pneumocystis jirovecii* infection[11]. The

specificity of this finding depends on the prior probability of COVID-19 based on molecular detection *via* polymerase chain reaction (PCR).

Reversed halo sign

The reversed halo sign is a focal ring-shaped area of ground-glass opacity within a peripheral rim of consolidation, suggesting an organizing/healing pneumonia[12]. It offers prognostic potential in COVID-19[13,14]. Data on sensitivity/specificity are not currently available. Utilizing classic signs of infarcts and pneumonia will increase diagnostic accuracy, and also help raise awareness about chest radiographs' utility, even in the current era, especially in cost-constrained locales lacking sophisticated infrastructure. It will also help develop more accurate AI algorithms for diagnosis/prognosis of COVID-19. Co-occurrences of these signs are uncommon across COVID-19 patients: When seen in tandem, however, they may constitute a highly specific diagnostic signature. This speculation, of course, needs validation by larger studies.

ADDITIONAL ANNOTATION TO IMAGES

The paper's images[1] show the following (currently unannotated) features: Subpleural sparing, figures 4B just under arrow marked as ground glass opacities, 7C and 7F; Hampton's humps, figures 2E, 2F, 4B (marked as consolidation), 4C and 7A (larger, but fewer, in the right lung than left lung); Westermark sign, figure 2F; and pericardial air, figure 2C.

AMPLIFIED DISCUSSION OF CARDIOVASCULAR EFFECTS FROM COVID-19

Distribution of cardiovascular angiotensin-converting enzyme 2 receptors and pathophysiology impact

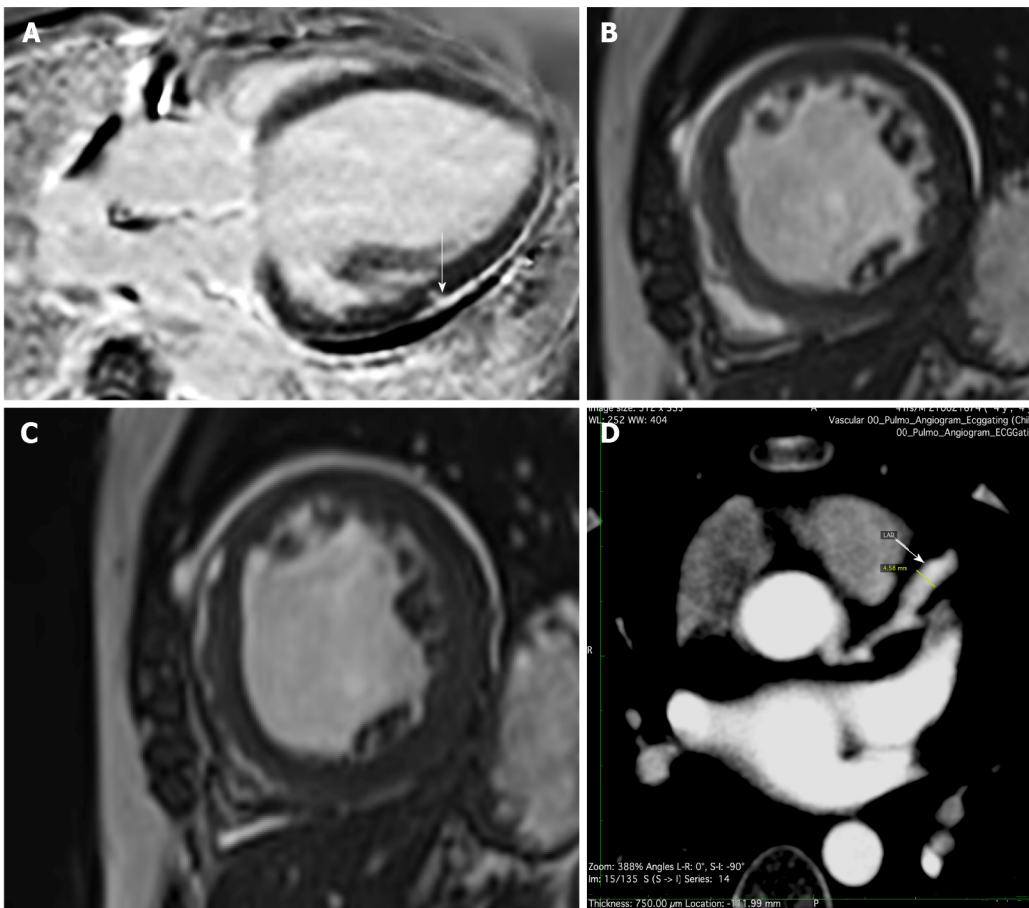
While correctly noting the ability of the severe acute respiratory syndrome coronavirus 2 (SARS-CoV-2), the causative agent of COVID-19, to invade cells by binding with high affinity to angiotensin-converting enzyme 2 and transmembrane protease serine 2 receptors, the authors have not discussed the cardiovascular system, where COVID-19's impact has been reviewed widely[6,15-17]. The angiotensin-converting enzyme 2 receptor is also expressed in the cardiovascular system in the endothelium of coronary arteries, cardiomyocytes, cardiac fibroblasts, epicardial adipocytes, vascular endothelial and smooth muscle cells[18-20].

Binding of SARS-CoV-2 to the endothelium predisposes to microthrombosis *via* endothelial inflammation, complement activation, thrombin generation, platelet and leukocyte recruitment and initiation of innate and adaptive immune responses with complications such as deep vein thrombosis, pulmonary embolism, cortical venous thrombosis, stroke, cardiac inflammation and injury, arrhythmias, blood clots [18] and acute/chronic myocardial injury[21]. An assay of the fibrin degradation product D-dimer (a thrombosis marker) on admission for prognostication of in-hospital mortality is now mandated in most clinical protocols to differentiate mild from severe COVID-19[7,22], especially when coupled with thrombocytopenia[8]. In infants and children reports of coronary artery aneurysms (CAA), including giant CAAs are gathering momentum as a part of multisystem inflammatory syndrome in post COVID-19 children[23-26].

ROLE OF CARDIAC AND THORACIC MAGNETIC RESONANCE IMAGING

While the authors correctly note that cardiac magnetic resonance imaging (MRI) may be useful in the future to detect complications in patients with abnormal echocardiography, this is a current need too. Up to 60% of hospitalized COVID-19 patients have been reported to have evidence of myocardial injury [21] (Figure 1A). Among post-discharge patients, approximately 10% complain of palpitations, with half of these having ongoing chest pain 6 mo after discharge[15]. Dilated cardiomyopathy is a known complication of COVID-19 cardiac injury[27] (Figures 1B and C). In post-COVID-vaccination patients, distinct self-limited myocarditis and pericarditis have appeared. While myocarditis developed rapidly in younger patients, mostly after the second vaccination, pericarditis affected older patients later, after either the first or second dose[28].

A recent report implicates the booster dose of the COVID-19 vaccine for acute myocarditis too[29]. In infants and children with COVID-19 reports of CAAs, including giant CAAs are gathering momentum [23-26], and cardiac MRI/CT can be an invaluable in diagnosing these too. This is particularly important as these aneurysms (and their catastrophic consequences) are potentially regressible with 'steroid therapy'. In addition these aneurysms would need to be monitored and managed, including for their potential to develop thrombosis[24]. Management includes cardiac support, immunomodulatory agents



DOI: 10.4329/wjr.v14.i9.342 Copyright ©The Author(s) 2022.

Figure 1 Post coronavirus disease 2019 imaging. A: Myocarditis: Magnetic resonance late gadolinium enhancement imaging, 4 chamber view. Subepicardial scar with focal myocardial extension (arrow) in the mid anterolateral segment of the left ventricle; B and C: Dilated cardiomyopathy: Bright blood T2 weighted cine imaging in short-axis 2 chamber view showing a dilated left ventricle. Patient had a history of coronavirus disease 2019 (COVID-19) infection a year ago followed by increasing dyspnea. Magnetic resonance imaging revealed severe left ventricular dysfunction and asynchronous left ventricle contractions, B: End diastole; C: End systole; D: Coronary artery aneurysm: Computed tomography angiography in a 4-year-old child reveals a fusiform aneurysm of the left anterior descending coronary artery (arrow). The patient had a history of COVID-19 8 mo ago and was following up for the same.

and anticoagulation[26]. Richardson *et al*[24] stated that in infants rapidly progressing CAAs are noted post COVID-19 infection. They also stated that as opposed to published reports these may be seen even in the absence of hemodynamic instability, ventricular dysfunction, myocardial ischemia or myopericarditis. In view of the risk of progression of cardiac signs and symptoms, Sperotto *et al*[26] recommended long-term follow-up of these patients. Coronary arteries should therefore be thoroughly assessed in patients presenting with multisystem inflammatory syndrome in children symptoms[25]. For its non-ionizing radiation nature MRI would be the first choice in children. However, CT on account of its speed (and current low radiation protocols) can be utilized effectively too (Figure 1D).

In their Radiology 2021 editorial, Lima *et al*[30] stated that prolonged symptoms due to “long-haul” COVID-19 portend the potential for chronic cardiac sequelae, whose duration and severity remain unknown. They introduced the work of Kravchenko *et al*[31], which demonstrated the value of cardiac MRI in identifying inflammation, adverse patterns of hypertrophy, fibrosis and myocardial injury due to myocarditis, pericarditis, cardiomyopathy and healing.

Although thoracic CT is widely used for imaging of COVID-19 infection, thoracic MRI can also be used as an alternative diagnostic tool because of its advantages[32]. This is particularly important in patients requiring avoidance of exposure to ionizing radiation, *e.g.*, in children and during pregnancy where pulmonary MRI may be preferred over pulmonary CT[33]. Pulmonary abnormalities caused by COVID-19 pneumonia can be detected on True FISP MRI sequences and correspond to the patterns known from CT. Spiro *et al*[34] made a useful suggestion for the current pandemic: Following MRI of the abdomen or heart, there should be careful evaluation of the visualized parts of the lungs for COVID-19 findings. This would enable the identification and isolation of undetected cases of COVID-19.

Necker *et al*[35] reported a cinematic rendering of SARS-CoV-2 pneumonia. Cinematic rendering is a digital three-dimensional visualization technique that converts grayscale slices from CT or MRI into colored three-dimensional volumes *via* transfer functions illuminating the reconstruction with physical light simulation. They have stated that this type of rendering produces a natural, photorealistic image

that is intuitively understandable and can be well applied for clinical purposes. Cinematic rendering of CT images is a new way to show the three dimensionality of the various densities contained in volumetric CT/MRI data. We agree with them and feel that such cinematic rendering can make complicated volume rendered CT/MRI images easy to understand for other clinicians, administrators, policy makers as well as patients alike.

ROLE OF 18-FLUORODEOXYGLUCOSE POSITRON EMISSION TOMOGRAPHY

The authors' suggestion of using fluorodeoxyglucose-positron emission tomography (PET) in the future for prognosis and monitoring is wonderful. We wish to add that the "rim sign", a slight and continuous fluorodeoxyglucose uptake at the border of a peripheral lung consolidation[36], is easily recognizable on fluorodeoxyglucose PET/CT (though data on sensitivity/specificity are not available). When present, it strongly suggests pulmonary infarction and is observable even without suggestive finding of pulmonary infarction. The reverse halo sign would also be seen. Though highly sensitive, use of PET/CT for primary detection of COVID-19 is constrained by poor specificity as well as considerations of cost, radiation burden and prolonged exposure times for imaging staff. However, in patients who may require nuclear medicine studies for other clinical indications, PET imaging may yield the earliest detection of nascent infection in otherwise asymptomatic individuals. This may be extremely vital for immunocompromised patients, including those with coexistent malignancies, where the early diagnosis of infection and subsequent initiation of care needed will contribute vitally to improving outcomes and reducing morbidity and mortality[33].

Role of optical thermal imaging and other remote patient monitoring devices

Lukose *et al*[37] stated that the currently popular method of collecting samples using the nasopharyngeal swab and subsequent detection of RNA using real-time PCR has false-positive results and a longer diagnostic time frame. Various optical techniques such as optical sensing, spectroscopy and imaging show great promise in virus detection, and the progress in the field of optical techniques for virus detection unambiguously show great promise in the development of rapid photonics-based devices for COVID-19 detection. They also provided a comprehensive review of the various photonics technologies employed for virus detection, especially the SARS-CoV family, such as near-infrared spectroscopy, fourier transform infrared spectroscopy, raman spectroscopy, fluorescence-based techniques, super-resolution microscopy and surface plasmon resonance-based detection.

Gomez-Gonzalez *et al*[38] reported a proof of concept of optical imaging spectroscopy for rapid, primary screening of SARS-CoV-2. A study by Shah *et al*[39] found that home pulse oximetry monitoring identified the need for hospitalization in initially non-severe COVID-19 patients when a cutoff SpO₂ of 92% was used and that home SpO₂ monitoring also reduced unnecessary emergency department revisits. McKay *et al*[40] stated that due to its portability, affordability and potential to serve as a screening tool for a conventionally lab-based invasive test, the mobile phone capillaroscope could serve as an important point-of-care tool and that the simplicity and portability of their technique may enable the development of an effective non-invasive tool for white blood cell screening in point-of-care and global health settings. This would be extremely useful in the COVID-19 pandemic scenario as white blood cell monitoring forms an essential part of COVID-19 management and follow-up[41,42].

Infrared thermography has been considered a gold standard method for screening febrile individuals during pandemics since the SARS outbreak in 2003. Khaksari *et al*[43] showed that in addition to an elevated body temperature a patient with COVID-19 will exhibit changes in other parameters such as oxygenation of tissues and cardiovascular and respiratory system functions. They also promulgated a compelling need to develop a new technique that would have the ability to screen all these signals and utilize the same for early detection of viral infections. In their opinion, keeping the advent of wireless technologies in mind, the development of such sensors that have point-of-care home-accessible capabilities will go a long way in better managing the increasing numbers of patients with COVID-19 who are opting for home quarantine and that this will eventually reduce the burden on the healthcare system.

The COVID-19 pandemic is changing the landscape of healthcare delivery worldwide. There is a discernible shift toward remote patient monitoring. It is pertinent to note that a large number of remote patient monitoring platforms are already utilizing optical technologies[44]. This area of research has great potential for growth, and the biomedical optics community has great prospects in the development, testing and commodification of new wearable remote patient monitoring technologies to add to the available healthcare armamentarium and contribute to the rapidly changing healthcare and research environment, not just for the COVID-19 era but far beyond[44].

Various other ingenious methods/modalities have been used for early detection/screening for COVID-19. These include smartwatches[45], smart phones and other intelligent edge devices. Mishra *et al*[45] developed a method utilizing data from smartwatches to detect the onset of COVID-19 infection in real-time that detected 67% of infection cases at or before symptom onset. They stated that their study provided a roadmap to a rapid and universal diagnostic method for the large-scale detection of

respiratory viral infections in advance of symptoms, highlighting a useful approach for managing epidemics using digital tracking and health monitoring. Seshadri *et al*[46] stated that when used in conjunction with predictive platforms, wearable device users could receive alerts when changes in their metrics match those related to COVID-19 and that such anonymous data localized to regions such as neighborhoods or zip codes could provide public health officials and researchers a valuable tool to track and mitigate the spread of the virus. Their manuscript describes clinically relevant physiological metrics that can be measured from commercial devices today and highlights their role in tracking the health, stability, and recovery of COVID-19 + individuals and front-line workers.

Schuller *et al*[47] in their paper titled 'COVID-19 and Computer Audition: An Overview on What Speech & Sound Analysis Could Contribute in the SARS-CoV-2 Corona Crisis' provided an overview on the potential for computer audition, *i.e.*, the usage of speech and sound analysis by AI, to help in the COVID-19 pandemic scenario and concluded that computer audition appears ready for implementation of (pre-)diagnosis and monitoring tools and more generally provides rich and significant, yet so far untapped, potential in the fight against COVID-19 spread.

AI in COVID-19 imaging. Telemedicine has advanced by leaps and bounds. AI algorithms enable faster diagnosis (including remote diagnosis), with a fair degree of accuracy[48]. While the application of AI to medical imaging of cancers and other diseases is being developed over the past decades, the recent COVID-19 pandemic hastened the: (1) Need; (2) Development; (3) Training; and (4) Testing of AI algorithms, within a relatively shorter time-span of less than 2 years[49]. This was extremely beneficial for radiologists and other physicians involved in performing rapid diagnosis, keeping in mind this was a time when there was immense overloading of the healthcare system[50]. The benefits including for management were obvious. However limitations such as: (1) Limited datasets; (2) Inaccurate execution of training and testing procedures; and (3) Use of incorrect performance criteria needed to be dealt with. The above limitations can be overcome by the utilization of federated learning[48,51,52].

The technique of federated learning was originally pioneered by Google[53] as an application of their well-known MapReduce algorithm[54] and allows for iteratively training a machine learning model across geographically separated hardware, including mobile devices. The machine learning algorithm is distributed, while data remains local. It can be employed for both statistical and deep learning. Despite its drawbacks, specifically wide-area network bandwidth limits computation speed, federated learning appears to be a great way forward, especially for multicenter collaborations, getting around the 'tricky' data privacy issue and enabling algorithms/outcomes with much more accuracy than otherwise possible[51].

If AI is to make an even greater impact, Merchant *et al*[48] suggested getting down to the basics and incorporating time tested key medical 'teaching' and/or key 'clinical' parameters, including prognostic indicators, for more effective AI algorithms and their better clinical utility. They also stated that "Artificial Intelligence needs real Intelligence to guide it!". Combining the wisdom gained over the years with the immense versatility of AI algorithms will maximize the accuracy and utility of AI applications in medical diagnosis and treatment modalities. We have gained wisdom regarding COVID-19 imaging over the past few years and should utilize the same for creation of better algorithms for screening/detection/prognostication and management.

El Naqa *et al*[55], as part of a Medical Imaging Data and Resource Center initiative, noted that the pandemic has led to the coupling of interdisciplinary experts that include: (1) Clinicians; (2) Medical physicists; (3) Imaging scientists; (4) Computer scientists; and (5) Informatics experts, all of whom are working towards solving the challenges of the COVID-19 pandemic, specifically AI methods applied to medical imaging. They stated that the lessons learned during the transitioning to AI in the medical imaging of COVID-19 can inform and enhance future AI applications, making the entire transition more than every discipline combined to respond to emergencies like the COVID-19 pandemic. AI has been used in multiple imaging fields for COVID-19 imaging.

The model by Manokaran *et al*[56] could achieve an accuracy of 94.00% in detecting COVID-19 and an overall accuracy of 92.19%, which was based on DenseNet-201. The model can achieve an area under receiver operating characteristic curve of 0.99 for COVID-19, 0.97 for normal and 0.97 for pneumonia. Their automated diagnostic model yielded an accuracy of 94.00% in the initial screening of COVID-19 patients and an overall accuracy of 92.19% using chest X-ray images.

Kusakunniran *et al*[57] proposed a solution to automatically classify COVID-19 cases in chest X-ray images using the ResNet-101 architecture, which was adopted as the main network with over 44 million parameters. A heatmap was constructed under the region of interest of the lung segment to visualize and emphasize signals of COVID-19. Their method achieved a sensitivity, specificity and accuracy of 97%, 98% and 98%, respectively. Rao *et al*[58] stated that separable SVNet and separable SVDNet models greatly reduced the number of parameters while improving the accuracy and increasing the operating speed.

Yi *et al*[50] utilized a large CT database (1112 patients) provided by the China Consortium of Chest CT Image Investigation and investigated multiple solutions in detecting COVID-19 and distinguishing it from other common pneumonia and normal controls. They compared the performance of different models for complete and segmented CT slices, in particular studying the effects of CT-superimposition depths into volumes, on the performance of their models and showed that an optimal model could identify COVID-19 slices with 99.76% accuracy (99.96% recall, 99.35% precision and 99.65% F1-score).

Chaddad *et al*[59] investigated the potential of deep transfer learning to predict COVID-19 infection using chest CT and X-ray images. They opined that combining chest CT and X-ray images with DarkNet architecture achieved the highest accuracy of 99.09% and area under receiver operating characteristic curve of 99.89% in classifying COVID-19 from non-COVID-19 and that their results confirmed the ability of deep convolutional neural networks with transfer learning to predict COVID-19 in both chest CT and X-ray images. They concluded that this approach could help radiologists improve the accuracy of their diagnosis and improve overall efficiency of COVID-19 management.

Cho *et al*[60] performed quantitative CT analysis on chest CT images using supervised machine learning to measure regional ground glass opacities and inspiratory and expiratory image matching to measure regional air trapping in survivors of COVID-19. They summarized that quantitative analysis of expiratory chest CT images demonstrated that small airway disease with the presence of air trapping is a long-lasting sequelae of SARS-CoV-2 infection.

Fuhrman *et al*[61] developed a cascaded transfer learning approach to extract quantitative features from thoracic CT sections using a fine-tuned VGG19 network where a CT-scan-level representation of thoracic characteristics and a support vector machine was trained to distinguish between patients who required steroid administration and those who did not. They demonstrated significant differences between patients who received steroids and those who did not and concluded that their 'cascade deep learning method' has great potential in clinical decision-making and for monitoring patient treatment.

THE FUTURE

Quantum computers and quantum microscopes, new quantum repeaters enabling a scalable super secure quantum internet (distance will no longer be a hindrance, not just internet of things but 'intelligent edge' devices commonplace[62]) will give a quantum boost to COVID-19 and other health care algorithms/strategies, including in other related fields, improving healthcare in ways beyond the realm of dreams[51]. Cloud computing could be complemented by edge computing, taking advantage of the burgeoning intelligent edge devices (smartphones are commonplace in the remotest of locations). Besides latency, edge computing is preferred over cloud computing in remote locations, where there is limited or no connectivity to a centralized location (a requirement of cloud computing), which requires local storage, similar to a mini data center at their location[63]. Medical imaging including COVID-19/other pandemic imaging and AI will never be the same again, in the era of quantum computing and quantum AI imaging and health care will reach stratospheric levels and beyond[47].

Correction of "pulmonary destruction". The author's state: "The migration of fluid into the alveolar sacs is governed by the imbalance in Starling forces. The diffuse alveolar damage caused by the viral particles results in an increased capillary wall permeability (high k value), thereby increasing the force at which fluid migrates from the capillaries to the alveolar space." emphasis added. Surely the authors mean "rate" instead of "force". Permeability is the inverse of resistance. By analogy with Ohm's Law for electricity (current = voltage/resistance) or its equivalent for blood pressure (cardiac output = blood pressure/peripheral resistance), capillary outflow will increase under fixed/constant pressure if permeability increases.

We hope that this augmentation of the excellent review by Pal *et al*[1] will enhance your readers' ability to evaluate COVID-19 patients on imaging. COVID-19 is here to stay. Each effort at adding to the information available in the literature will go a long way in improving patient care overall.

FOOTNOTES

Author contributions: All authors contributed equally.

Conflict-of-interest statement: All the authors report no relevant conflicts of interest for this article.

Open-Access: This article is an open-access article that was selected by an in-house editor and fully peer-reviewed by external reviewers. It is distributed in accordance with the Creative Commons Attribution NonCommercial (CC BY-NC 4.0) license, which permits others to distribute, remix, adapt, build upon this work non-commercially, and license their derivative works on different terms, provided the original work is properly cited and the use is non-commercial. See: <https://creativecommons.org/licenses/by-nc/4.0/>

Country/Territory of origin: India

ORCID number: Suleman Adam Merchant 0000-0001-6513-450X; Prakash Nadkarni 0000-0002-9628-4700; Mohd Javed Saifullah Shaikh 0000-0002-5615-4813.

S-Editor: Wang JJ

L-Editor: Filipodia

P-Editor: Wang JJ

REFERENCES

- 1 **Pal A**, Ali A, Young TR, Oostenbrink J, Prabhakar A, Deacon N, Arnold A, Eltayeb A, Yap C, Young DM, Tang A, Lakshmanan S, Lim YY, Pokarowski M, Kakodkar P. Comprehensive literature review on the radiographic findings, imaging modalities, and the role of radiology in the COVID-19 pandemic. *World J Radiol* 2021; **13**: 258-282 [PMID: 34630913 DOI: 10.4329/wjr.v13.i9.258]
- 2 **Merchant SA**, Ansari SMS, Merchant N. Additional Chest Imaging Signs That Have the Potential of Being COVID-19 Imaging Markers. *AJR Am J Roentgenol* 2020; **215**: W57-W58 [PMID: 32762540 DOI: 10.2214/AJR.20.24170]
- 3 **Worsley DF**, Alavi A, Aronchick JM, Chen JT, Greenspan RH, Ravin CE. Chest radiographic findings in patients with acute pulmonary embolism: observations from the PIOPED Study. *Radiology* 1993; **189**: 133-136 [PMID: 8372182 DOI: 10.1148/radiology.189.1.8372182]
- 4 **Han D**, Lee KS, Franquet T, Müller NL, Kim TS, Kim H, Kwon OJ, Byun HS. Thrombotic and nonthrombotic pulmonary arterial embolism: spectrum of imaging findings. *Radiographics* 2003; **23**: 1521-1539 [PMID: 14615562 DOI: 10.1148/rg.1103035043]
- 5 **Stein PD**, Beemath A, Matta F, Weg JG, Yusen RD, Hales CA, Hull RD, Leeper KV Jr, Sostman HD, Tapson VF, Buckley JD, Gottschalk A, Goodman LR, Wakefield TW, Woodard PK. Clinical characteristics of patients with acute pulmonary embolism: data from PIOPED II. *Am J Med* 2007; **120**: 871-879 [PMID: 17904458 DOI: 10.1016/j.amjmed.2007.03.024]
- 6 **Madjid M**, Safavi-Naeini P, Solomon SD, Vardeny O. Potential Effects of Coronaviruses on the Cardiovascular System: A Review. *JAMA Cardiol* 2020; **5**: 831-840 [PMID: 32219363 DOI: 10.1001/jamacardio.2020.1286]
- 7 **Zhang L**, Yan X, Fan Q, Liu H, Liu X, Liu Z, Zhang Z. D-dimer levels on admission to predict in-hospital mortality in patients with Covid-19. *J Thromb Haemost* 2020; **18**: 1324-1329 [PMID: 32306492 DOI: 10.1111/jth.14859]
- 8 **McFadyen JD**, Stevens H, Peter K. The Emerging Threat of (Micro)Thrombosis in COVID-19 and Its Therapeutic Implications. *Circ Res* 2020; **127**: 571-587 [PMID: 32586214 DOI: 10.1161/CIRCRESAHA.120.317447]
- 9 **Léonard-Lorant I**, Delabranche X, Séverac F, Helms J, Pauzet C, Collange O, Schneider F, Labani A, Bilbault P, Molière S, Leyendecker P, Roy C, Ohana M. Acute Pulmonary Embolism in Patients with COVID-19 at CT Angiography and Relationship to d-Dimer Levels. *Radiology* 2020; **296**: E189-E191 [PMID: 32324102 DOI: 10.1148/radiol.2020201561]
- 10 **Tabatabaei SMH**, Talari H, Moghaddas F, Rajebi H. CT Features and Short-term Prognosis of COVID-19 Pneumonia: A Single-Center Study from Kashan, Iran. *Radiol Cardiothorac Imaging* 2020; **2**: e200130 [PMID: 33778569 DOI: 10.1148/ryct.2020200130]
- 11 **Chong WH**, Saha BK, Austin A, Chopra A. The Significance of Subpleural Sparing in CT Chest: A State-of-the-Art Review. *Am J Med Sci* 2021; **361**: 427-435 [PMID: 33487401 DOI: 10.1016/j.amjms.2021.01.008]
- 12 **Maturu VN**, Agarwal R. Reversed halo sign: a systematic review. *Respir Care* 2014; **59**: 1440-1449 [PMID: 24782557 DOI: 10.4187/respcare.03020]
- 13 **Sales AR**, Casagrande EM, Hochegger B, Zanetti G, Marchiori E. The Reversed Halo Sign and COVID-19: Possible Histopathological Mechanisms Related to the Appearance of This Imaging Finding. *Arch Bronconeumol* 2021; **57**: 73-75 [PMID: 34629671 DOI: 10.1016/j.arbres.2020.06.029]
- 14 **Marchiori E**, Nobre LF, Hochegger B, Zanetti G. CT characteristics of COVID-19: reversed halo sign or target sign? *Diagn Interv Radiol* 2021; **27**: 306-307 [PMID: 33290240 DOI: 10.5152/dir.2020.20734]
- 15 **Huang C**, Huang L, Wang Y, Li X, Ren L, Gu X, Kang L, Guo L, Liu M, Zhou X, Luo J, Huang Z, Tu S, Zhao Y, Chen L, Xu D, Li Y, Li C, Peng L, Xie W, Cui D, Shang L, Fan G, Xu J, Wang G, Zhong J, Wang C, Wang J, Zhang D, Cao B. 6-month consequences of COVID-19 in patients discharged from hospital: a cohort study. *Lancet* 2021; **397**: 220-232 [PMID: 33428867 DOI: 10.1016/S0140-6736(20)32656-8]
- 16 **Hamming I**, Timens W, Bulthuis ML, Lely AT, Navis G, van Goor H. Tissue distribution of ACE2 protein, the functional receptor for SARS coronavirus. A first step in understanding SARS pathogenesis. *J Pathol* 2004; **203**: 631-637 [PMID: 15141377 DOI: 10.1002/path.1570]
- 17 **Zheng YY**, Ma YT, Zhang JY, Xie X. COVID-19 and the cardiovascular system. *Nat Rev Cardiol* 2020; **17**: 259-260 [PMID: 32139904 DOI: 10.1038/s41569-020-0360-5]
- 18 **Salamanna F**, Maglio M, Landini MP, Fini M. Body Localization of ACE-2: On the Trail of the Keyhole of SARS-CoV-2. *Front Med (Lausanne)* 2020; **7**: 594495 [PMID: 33344479 DOI: 10.3389/fmed.2020.594495]
- 19 **Gheblawi M**, Wang K, Viveiros A, Nguyen Q, Zhong JC, Turner AJ, Raizada MK, Grant MB, Oudit GY. Response by Gheblawi et al to Letter Regarding Article, "Angiotensin-Converting Enzyme 2: SARS-CoV-2 Receptor and Regulator of the Renin-Angiotensin System: Celebrating the 20th Anniversary of the Discovery of ACE2". *Circ Res* 2020; **127**: e46-e47 [PMID: 32614719 DOI: 10.1161/CIRCRESAHA.120.317332]
- 20 **Patel VB**, Zhong JC, Grant MB, Oudit GY. Role of the ACE2/Angiotensin 1-7 Axis of the Renin-Angiotensin System in Heart Failure. *Circ Res* 2016; **118**: 1313-1326 [PMID: 27081112 DOI: 10.1161/CIRCRESAHA.116.307708]
- 21 **Giustino G**, Croft LB, Stefanini GG, Bragato R, Silbiger JJ, Vicenzi M, Danilov T, Kukar N, Shaban N, Kini A, Camaj A, Bienstock SW, Rashed ER, Rahman K, Oates CP, Buckley S, Elbaum LS, Arkonac D, Fiter R, Singh R, Li E, Razuk V, Robinson SE, Miller M, Bier B, Donghi V, Pisaniello M, Mantovani R, Pinto G, Rota I, Baggio S, Chiarito M, Fazzari F, Cusmano I, Curzi M, Ro R, Malick W, Kamran M, Kohli-Seth R, Bassily-Marcus AM, Neibart E, Serrao G, Perk G, Mancini D, Reddy VY, Pinney SP, Dangas G, Blasi F, Sharma SK, Mehran R, Condorelli G, Stone GW, Fuster V, Lerakis S, Goldman ME. Characterization of Myocardial Injury in Patients With COVID-19. *J Am Coll Cardiol* 2020; **76**: 2043-2055 [PMID: 33121710 DOI: 10.1016/j.jacc.2020.08.069]
- 22 **Velavan TP**, Meyer CG. Mild versus severe COVID-19: Laboratory markers. *Int J Infect Dis* 2020; **95**: 304-307 [PMID: 32344011 DOI: 10.1016/j.ijid.2020.04.061]

- 23 **Navaeifar MR**, Shahbaznejad L, Sadeghi Lotfabadi A, Rezai MS. COVID-19-Associated Multisystem Inflammatory Syndrome Complicated with Giant Coronary Artery Aneurysm. *Case Rep Pediatr* 2021; **2021**: 8836403 [PMID: [33505752](#) DOI: [10.1155/2021/8836403](#)]
- 24 **Richardson KL**, Jain A, Evans J, Uzun O. Giant coronary artery aneurysm as a feature of coronavirus-related inflammatory syndrome. *BMJ Case Rep* 2021; **14** [PMID: [34210694](#) DOI: [10.1136/bcr-2020-238740](#)]
- 25 **Pick JM**, Wang S, Wagner-Lees S, Badran S, Szmuszkovicz JR, Wong P, Votava-Smith J. Abstract 17092: Coronary Artery Aneurysms Are More Common in Post-COVID-19 Multisystem Inflammatory Syndrome in Children (MIS-C) Than Pre-Pandemic Kawasaki Disease. *Circulation* 2020; **142**: A17092 [DOI: [10.1161/circ.142.suppl_3.17092](#)]
- 26 **Sperotto F**, Friedman KG, Son MBF, VanderPluym CJ, Newburger JW, Dionne A. Cardiac manifestations in SARS-CoV-2-associated multisystem inflammatory syndrome in children: a comprehensive review and proposed clinical approach. *Eur J Pediatr* 2021; **180**: 307-322 [PMID: [32803422](#) DOI: [10.1007/s00431-020-03766-6](#)]
- 27 **Omidif F**, Hajikhani B, Kazemi SN, Tajbakhsh A, Riazzi S, Mirsaedi M, Ansari A, Ghanbari Boroujeni M, Khalili F, Hadadi S, Nasiri MJ. COVID-19 and Cardiomyopathy: A Systematic Review. *Front Cardiovasc Med* 2021; **8**: 695206 [PMID: [34222385](#) DOI: [10.3389/fcvm.2021.695206](#)]
- 28 **Diaz GA**, Parsons GT, Gering SK, Meier AR, Hutchinson IV, Robicsek A. Myocarditis and Pericarditis After Vaccination for COVID-19. *JAMA* 2021; **326**: 1210-1212 [PMID: [34347001](#) DOI: [10.1001/jama.2021.13443](#)]
- 29 **Sanchez Tijmes F**, Zamorano A, Thavendiranathan P, Hanneman K. Imaging of Myocarditis Following mRNA COVID-19 Booster Vaccination. *Radiol Cardiothorac Imaging* 2022; **4**: e220019 [PMID: [35506135](#) DOI: [10.1148/ryct.220019](#)]
- 30 **Lima JAC**, Bluemke DA. Myocardial Scar in COVID-19: Innocent Marker versus Harbinger of Clinical Disease. *Radiology* 2021; **301**: E434-E435 [PMID: [34374597](#) DOI: [10.1148/radiol.2021211710](#)]
- 31 **Kravchenko D**, Isaak A, Zimmer S, Mesropyan N, Reinert M, Faron A, Pieper CC, Heine A, Velten M, Nattermann J, Kuetting D, Duerr GD, Attenberger UI, Luetkens JA. Cardiac MRI in Patients with Prolonged Cardiorespiratory Symptoms after Mild to Moderate COVID-19. *Radiology* 2021; **301**: E419-E425 [PMID: [34374593](#) DOI: [10.1148/radiol.2021211162](#)]
- 32 **Ates OF**, Taydas O, Dheir H. Thorax Magnetic Resonance Imaging Findings in Patients with Coronavirus Disease (COVID-19). *Acad Radiol* 2020; **27**: 1373-1378 [PMID: [32830031](#) DOI: [10.1016/j.acra.2020.08.009](#)]
- 33 **Fields BKK**, Demirjian NL, Dadgar H, Gholamrezaezhad A. Imaging of COVID-19: CT, MRI, and PET. *Semin Nucl Med* 2021; **51**: 312-320 [PMID: [33288215](#) DOI: [10.1053/j.semnuclmed.2020.11.003](#)]
- 34 **Spiro JE**, Curta A, Mansournia S, Marschner CA, Maurus S, Weckbach LT, Hedderich DM, Dinkel J. Appearance of COVID-19 pneumonia on 1.5 T TrueFISP MRI. *Radiol Bras* 2021; **54**: 211-218 [PMID: [34393286](#) DOI: [10.1590/0100-3984.2021.0028](#)]
- 35 **Necker FN**, Scholz M. Chest CT Cinematic Rendering of SARS-CoV-2 Pneumonia. *Radiology* 2022; **303**: 501 [PMID: [34935512](#) DOI: [10.1148/radiol.212902](#)]
- 36 **Soussan M**, Rust E, Pop G, Morère JF, Brilllet PY, Eder V. The rim sign: FDG-PET/CT pattern of pulmonary infarction. *Insights Imaging* 2012; **3**: 629-633 [PMID: [22903456](#) DOI: [10.1007/s13244-012-0189-5](#)]
- 37 **Lukose J**, Chidangil S, George SD. Optical technologies for the detection of viruses like COVID-19: Progress and prospects. *Biosens Bioelectron* 2021; **178**: 113004 [PMID: [33497877](#) DOI: [10.1016/j.bios.2021.113004](#)]
- 38 **Gomez-Gonzalez E**, Barriga-Rivera A, Fernandez-Muñoz B, Navas-Garcia JM, Fernandez-Lizaranzu I, Munoz-Gonzalez FJ, Parrilla-Giraldez R, Requena-Lancharro D, Gil-Gamboa P, Rosell-Valle C, Gomez-Gonzalez C, Mayorga-Buiza MJ, Martin-Lopez M, Muñoz O, Gomez-Martin JC, Relimpio-Lopez MI, Aceituno-Castro J, Perales-Esteve MA, Puppò-Moreno A, Garcia-Cozar FJ, Olvera-Collantes L, Gomez-Diaz R, de Los Santos-Trigo S, Huguet-Carrasco M, Rey M, Gomez E, Sanchez-Pernaute R, Padillo-Ruiz J, Marquez-Rivas J. Optical imaging spectroscopy for rapid, primary screening of SARS-CoV-2: a proof of concept. *Sci Rep* 2022; **12**: 2356 [PMID: [35181702](#) DOI: [10.1038/s41598-022-06393-3](#)]
- 39 **Shah S**, Majmudar K, Stein A, Gupta N, Suppes S, Karamanis M, Capannari J, Sethi S, Patte C. Novel Use of Home Pulse Oximetry Monitoring in COVID-19 Patients Discharged From the Emergency Department Identifies Need for Hospitalization. *Acad Emerg Med* 2020; **27**: 681-692 [PMID: [32779828](#) DOI: [10.1111/acem.14053](#)]
- 40 **McKay GN**, Mohan N, Butterworth I, Bourquard A, Sánchez-Ferro Á, Castro-González C, Durr NJ. Visualization of blood cell contrast in nailfold capillaries with high-speed reverse lens mobile phone microscopy. *Biomed Opt Express* 2020; **11**: 2268-2276 [PMID: [32341882](#) DOI: [10.1364/BOE.382376](#)]
- 41 **Pirsalehi A**, Salari S, Baghestani A, Sanadgol G, Shirini D, Baerz MM, Abdi S, Akbari ME, Bashash D. Differential alteration trend of white blood cells (WBCs) and monocytes count in severe and non-severe COVID-19 patients within a 7-day follow-up. *Iran J Microbiol* 2021; **13**: 8-16 [PMID: [33889357](#) DOI: [10.18502/ijm.v13i1.5486](#)]
- 42 **Leulseged TW**, Hassen IS, Ayele BT, Tsegay YG, Abebe DS, Edo MG, Maru EH, Zewde WC, Naylor LK, Semane DF, Dresse MT, Tezera BB. Laboratory biomarkers of COVID-19 disease severity and outcome: Findings from a developing country. *PLoS One* 2021; **16**: e0246087 [PMID: [33720944](#) DOI: [10.1371/journal.pone.0246087](#)]
- 43 **Khaksari K**, Nguyen T, Hill B, Quang T, Perreault J, Gorti V, Malpani R, Blick E, González Cano T, Shadgan B, Gandjbakhche AH. Review of the efficacy of infrared thermography for screening infectious diseases with applications to COVID-19. *J Med Imaging (Bellingham)* 2021; **8**: 010901 [PMID: [33786335](#) DOI: [10.1117/1.JMI.8.S1.010901](#)]
- 44 **Roblyer D**. Perspective on the increasing role of optical wearables and remote patient monitoring in the COVID-19 era and beyond. *J Biomed Opt* 2020; **25** [PMID: [33089674](#) DOI: [10.1117/1.JBO.25.10.102703](#)]
- 45 **Mishra T**, Wang M, Metwally AA, Bogu GK, Brooks AW, Bahmani A, Alavi A, Celli A, Higgs E, Dagan-Rosenfeld O, Fay B, Kirkpatrick S, Kellogg R, Gibson M, Wang T, Rolnik B, Ganz AB, Li X, Snyder MP. Early Detection Of COVID-19 Using A Smartwatch. 2020 Preprint. Available from: medRxiv: 2020.07.06.20147512 [DOI: [10.1101/2020.07.06.20147512](#)]
- 46 **Seshadri DR**, Davies EV, Harlow ER, Hsu JJ, Knighton SC, Walker TA, Voos JE, Drummond CK. Wearable Sensors for COVID-19: A Call to Action to Harness Our Digital Infrastructure for Remote Patient Monitoring and Virtual Assessments. *Front Digit Health* 2020; **2**: 8 [PMID: [34713021](#) DOI: [10.3389/fdgh.2020.00008](#)]
- 47 **Schuller BW**, Schuller DM, Qian K, Liu J, Zheng H, Li X. COVID-19 and Computer Audition: An Overview on What Speech & Sound Analysis Could Contribute in the SARS-CoV-2 Corona Crisis. *Front Digit Health* 2021; **3**: 564906

- [PMID: 34713079 DOI: 10.3389/fdth.2021.564906]
- 48 **Merchant SA**, Shaikh MJS, Nadkarni P. Tuberculosis conundrum - current and future scenarios: A proposed comprehensive approach combining laboratory, imaging, and computing advances. *World J Radiol* 2022; **14**: 114-136 [DOI: 10.4329/wjr.v14.i6.114]
 - 49 **Giger M**. Medical imaging of COVID-19. *J Med Imaging (Bellingham)* 2021; **8**: 010101 [PMID: 34754885 DOI: 10.1117/1.JMI.8.S1.010101]
 - 50 **Li Y**, Pei X, Guo Y. 3D CNN classification model for accurate diagnosis of coronavirus disease 2019 using computed tomography images. *J Med Imaging (Bellingham)* 2021; **8**: 017502 [PMID: 34322573 DOI: 10.1117/1.JMI.8.S1.017502]
 - 51 **Nadkarni P**, Merchant SA. Enhancing medical-imaging artificial intelligence through holistic use of time-tested key imaging and clinical parameters: Future insights. *Artif Intell Med Imaging* 2022; **3**: 55-69 [DOI: 10.35711/aimi.v3.i3.55]
 - 52 **Rieke N**, Hancox J, Li W, Milletari F, Roth HR, Albarqouni S, Bakas S, Galtier MN, Landman BA, Maier-Hein K, Ourselin S, Sheller M, Summers RM, Trask A, Xu D, Baust M, Cardoso MJ. The future of digital health with federated learning. *NPJ Digit Med* 2020; **3**: 119 [PMID: 33015372 DOI: 10.1038/s41746-020-00323-1]
 - 53 **McMahan B**, Ramage D. Federated Learning: Collaborative Machine Learning without Centralized Training Data. Google AI Blog. 6 Apr 2017. [cited 14 November 2021]. Available from: <https://starrymind.tistory.com/180>
 - 54 **Dean J**, Ghemawat S. MapReduce: Simplified Data Processing on Large Clusters. *Commun ACM* 2008; **51**: 107-113 [DOI: 10.1145/1327452.1327492]
 - 55 **El Naqa I**, Li H, Fuhrman J, Hu Q, Gorre N, Chen W, Giger ML. Lessons learned in transitioning to AI in the medical imaging of COVID-19. *J Med Imaging (Bellingham)* 2021; **8**: 010902-010902 [PMID: 34646912 DOI: 10.1117/1.JMI.8.S1.010902]
 - 56 **Manokaran J**, Zabihollahy F, Hamilton-Wright A, Ukwatta E. Detection of COVID-19 from chest x-ray images using transfer learning. *J Med Imaging (Bellingham)* 2021; **8**: 017503 [PMID: 34435075 DOI: 10.1117/1.JMI.8.S1.017503]
 - 57 **Kusakunniran W**, Karnjanapreechakorn S, Siriapisith T, Borwarnginn P, Sutassananon K, Tongdee T, Saiviroonporn P. COVID-19 detection and heatmap generation in chest x-ray images. *J Med Imaging (Bellingham)* 2021; **8**: 014001 [PMID: 33457446 DOI: 10.1117/1.JMI.8.S1.014001]
 - 58 **Rao K**, Xie K, Hu Z, Guo X, Wen C, He J. COVID-19 detection method based on SVRNet and SVDNet in lung x-rays. *J Med Imaging (Bellingham)* 2021; **8**: 017504 [PMID: 34471647 DOI: 10.1117/1.JMI.8.S1.017504]
 - 59 **Chaddad A**, Hassan L, Desrosiers C. Deep CNN models for predicting COVID-19 in CT and x-ray images. *J Med Imaging (Bellingham)* 2021; **8**: 014502 [PMID: 33912622 DOI: 10.1117/1.JMI.8.S1.014502]
 - 60 **Cho JL**, Villacreses R, Nagpal P, Guo J, Pezzulo AA, Thurman AL, Hamzeh NY, Blount RJ, Fortis S, Hoffman EA, Zabner J, Comellas AP. Quantitative Chest CT Assessment of Small Airways Disease in Post-Acute SARS-CoV-2 Infection. *Radiology* 2022; **304**: 185-192 [PMID: 35289657 DOI: 10.1148/radiol.212170]
 - 61 **Fuhrman JD**, Chen J, Dong Z, Lure FYM, Luo Z, Giger ML. Cascaded deep transfer learning on thoracic CT in COVID-19 patients treated with steroids. *J Med Imaging (Bellingham)* 2021; **8**: 014501 [PMID: 33415179 DOI: 10.1117/1.JMI.8.S1.014501]
 - 62 **TechCrunch BS**. The future is not the Internet of Things... it is the Connected Intelligent Edge. Dec 21, 2021. [cited 22 December 2021]. Available from: <https://www.nastel.com/the-future-is-not-the-internet-of-things-it-is-the-connected-intelligent-edge/>
 - 63 **Arora S**. Edge Computing Vs. Cloud Computing: What are the Differences. Jun 30, 2022. [cited 8 March 2022]. Available from: <https://www.simplilearn.com/edge-computing-vs-cloud-computing-article>



Published by **Baishideng Publishing Group Inc**
7041 Koll Center Parkway, Suite 160, Pleasanton, CA 94566, USA
Telephone: +1-925-3991568
E-mail: bpgoffice@wjgnet.com
Help Desk: <https://www.f6publishing.com/helpdesk>
<https://www.wjgnet.com>

